Preprints.org

Article

Not peer-reviewed version

Source-Specific Photobiomodulation Regulates Mitochondrial Bioenergetics, Redox Signaling, and Functional Outputs in C2C12 Myoblasts Across Replicative Aging

Ana Elena Aviña , Nguyen Le Thanh Hang , Che-Yi Chang , Yi-Fan Chen , Yun Yen , Xavier Pei-Chun Wong , Aline Yen Ling Wang , Cheng-Jen Chang * , Tzu-Sen Yang *

Posted Date: 5 February 2026

doi: 10.20944/preprints202602.0413.v1

Keywords: photobiomodulation; muscle; aging; C2C12 myoblasts; mitochondria; reactive oxygen species; extracellular vesicles; bioenergetics; NIR; LED

Preprints.org is a free multidisciplinary platform providing preprint service that is dedicated to making early versions of research outputs permanently available and citable. Preprints posted at Preprints.org appear in Web of Science, Crossref, Google Scholar, Scilit, Europe PMC.

Copyright: This open access article is published under a Creative Commons CC BY 4.0 license, which permit the free download, distribution, and reuse, provided that the author and preprint are cited in any reuse.

Preprints.org (www.preprints.org) | NOT PEER-REVIEWED | Posted: 5 February 2026 doi:10.20944/preprints202602.0413.v1

Disclaimer/Publisher's Note: The statements, opinions, and data contained in all publications are solely those of the individual author(s) and contributor(s) and not of MDPI and/or the editor(s). MDPI and/or the editor(s) disclaim responsibility for any injury to people or property resulting from any ideas, methods, instructions, or products referred to in the content.

Article

Source-Specific Photobiomodulation Regulates Mitochondrial Bioenergetics, Redox Signaling, and Functional Outputs in C2C12 Myoblasts Across Replicative Aging

Ana Elena Aviña [1,2,3,4], Nguyen Le Thanh Hang [2,5], Che-Yi Chang [6], Yi-Fan Chen [7,8], Yun Yen [8], Xavier Pei-Chun Wong [2,9], Aline Yen Ling Wang [4], Cheng-Jen Chang [2,3,10,*] and Tzu-Sen Yang [2,9,11,12,13,*]

1 International Ph.D. Program in Medicine, College of Medicine, Taipei Medical University, Taipei 110, Taiwan
2 Graduate Institute of Biomedical Optomechatronics, College of Biomedical Engineering, Taipei Medical University, New Taipei City 235, Taiwan
3 Department of Plastic Surgery, Taipei Medical University Hospital, Taipei Medical University, Taipei 110, Taiwan
4 Center for Vascularized Composite Allotransplantation, Chang Gung Memorial Hospital, Taoyuan 333, Taiwan
5 Department of Otolaryngology, National Taiwan University Hospital, Taipei 100, Taiwan
6 Graduate Institute of Biomedical Materials and Tissue Engineering, Taipei Medical University, Taipei 110, Taiwan
7 International Master/Ph.D. Program for Translation Science, College of Medical Science and Technology, Taipei Medical University, New Taipei City 235, Taiwan
8 TMU Research Center of Cancer Translational Medicine, Taipei Medical University, Taipei 110, Taiwan
9 College of Biomedical Engineering, Taipei Medical University, New Taipei City 235, Taiwan
10 Department of Surgery, School of Medicine, College of Medicine, Taipei Medical University, Taipei 110, Taiwan
11 International Ph.D. Program in Biomedical Engineering, Taipei Medical University, New Taipei City 235, Taiwan
12 School of Dental Technology, Taipei Medical University, Taipei 110, Taiwan
13 Research Center of Biomedical Devices, Taipei Medical University, Taipei 110, Taiwan
* Correspondence: chengjen@h.tmu.edu.tw (C.-J.C.), tsyang@tmu.edu.tw (T.-S.Y)

Abstract

Age-related muscle decline is associated with impaired mitochondrial bioenergetics, altered redox signaling, and reduced myogenic capacity, yet how photobiomodulation (PBM) source characteristics shape these processes under replicative aging remains unclear. Here, we investigated source-specific PBM responses in C2C12 myoblasts using a 660 nm light-emitting diode (LED) and an 830 nm near-infrared (NIR) laser across fluence ranges and replicative stages. Single-cell screening performed at passage 25 identified 5 J/cm² as the optimal fluence for both sources, producing biphasic increases in mitochondrial membrane potential and ROS. Population-level assays in young (≤5 passages) and old (≥30 passages) cells revealed divergent downstream outcomes. LED irradiation elicited stronger metabolic activation and ATP production, particularly in aged cells, whereas NIR irradiation robustly enhanced myogenic fusion in both age groups and partially rescued differentiation deficits in aged myoblasts. Bulk ROS increased significantly after PBM independent of source, while extracellular vesicle release displayed age-dependent source sensitivity, with NIR favoring canonical small EV populations in young cells and LED inducing greater particle release in aged cells. Together, these findings demonstrate that PBM engages

© 2025 by the author(s). Distributed under a Creative Commons CC BY license.

Preprints.org (www.preprints.org) | NOT PEER-REVIEWED | Posted: 5 February 2026 doi:10.20944/preprints202602.0413.v1

conserved mitochondrial signaling while source-specific delivery and wavelength differentially directs metabolic, paracrine, and myogenic outputs under replicative aging conditions.

Keywords: photobiomodulation; muscle; aging; C2C12 myoblasts; mitochondria; reactive oxygen species; extracellular vesicles; bioenergetics; NIR; LED

1. Introduction

Photobiomodulation (PBM) is a form of light therapy that employs non-ionizing light sources, including lasers, light-emitting diodes (LEDs), and broadband light, in the visible to near-infrared spectrum. It is a nonthermal process that elicits photophysical and photochemical events via endogenous chromophores, resulting in therapeutic outcomes such as tissue repair, immunomodulation, and improved cellular function [1,2]. Beyond its therapeutic scope, PBM has been increasingly explored for regenerative medicine applications, where it shows potential to enhance healing and modulate cellular communication.

Mitochondria, particularly cytochrome c oxidase (CcO) in complex IV of the electron transport chain, are widely recognized as key photoacceptors. Upon light absorption, CcO activity increases, leading to enhanced electron transport, elevated mitochondrial membrane potential [MMP ($\Delta\Psi m$)], and greater ATP production [3–6] Controlled reactive oxygen species (ROS) production may further serve as redox signals that regulate cell adaptation and repair [7–12]. These findings highlight the interplay between mitochondrial bioenergetics, $\Delta\Psi m$, and ROS as a central mechanism underlying PBM responses.

Because skeletal muscle is highly reliant on mitochondrial capacity for function and repair, PBM has been investigated for its ability to improve exercise performance, accelerate recovery, and mitigate fatigue [13,14]. Nevertheless, interpretability remains challenging: biological outcomes vary across studies depending on wavelength, fluence, source characteristics, and the biphasic dose-response phenomenon is well established in PBM [15,16]. Few studies have systematically linked mitochondrial responses to functional outputs such as migration, differentiation, or extracellular vesicle (EV) release within a single experimental platform [17–19].

This gap is particularly relevant to conditions of age-related muscle loss and weakness (such as sarcopenia) [20,21] in which mitochondrial bioenergetic dysfunction plays a central role. Impaired oxidative phosphorylation, reduced ATP production, and altered mitochondrial dynamics converge with defective myogenic differentiation and disrupted redox signaling, collectively driving the progressive decline of muscle mass and function. Beyond energy failure, mitochondria act as signaling hubs that regulate reactive oxygen species, calcium handling, and apoptotic pathways, meaning their dysfunction propagates systemic stress responses that accelerate tissue frailty. Understanding and targeting these interconnected processes is therefore critical for developing strategies to mitigate muscle aging and restore regenerative potential [21–24].

Accordingly, we selected two commonly used but physically distinct PBM sources: a red LED at 660 nm and a near-infrared (NIR) laser at 830 nm. These wavelengths were chosen not only because both fall within the “optical window” for tissue penetration, but also because their biological actions are complementary. Red light at 660 nm has a shallower penetration profile, favoring safe, broad-coverage stimulation of superficial or preventive targets, while 830 nm penetrates deeper and is better suited for modulating mitochondrial function in thicker tissue contexts [25–28]. The use of an LED at 660 nm represents a practical, safer, and more accessible source, while the coherent 830 nm laser provides higher photon density and depth, enabling a side-by-side comparison of how light source properties influence mitochondrial dynamics in the same cellular model [29,30].

The C2C12 myoblast line offers a robust system to explore these questions because it retains strong mitochondrial content, differentiates into multinucleated myotubes, and reproduces key features of muscle physiology [31,32]. Importantly, its well-documented passage-dependent changes allow comparisons between early-passage “young” cells, which maintain proliferative and

© 2025 by the author(s). Distributed under a Creative Commons CC BY license.

Preprints.org (www.preprints.org) | NOT PEER-REVIEWED | Posted: 5 February 2026 doi:10.20944/preprints202602.0413.v1

differentiation capacity, and late-passage "old" cells, which accumulate mitochondrial and functional deficits [33,34]. This makes C2C12 particularly suited to mechanistic interrogation of mitochondrial function under PBM, enabling quantitative single-cell readouts of ΔΨm and ROS, alongside functional assays of migration, differentiation, and EV release.

Here, we hypothesized that PBM delivered by LED and NIR laser sources at 660 nm and 830 nm, respectively, would differentially influence mitochondrial function of C2C12 myoblasts in a fluence-dependent manner, and that these mitochondrial responses would align with functional outputs relevant to myogenesis under replicative aging conditions. The novelty of this study lies in combining image-based single-cell mitochondrial assessments with bulk functional assays across early- and late-passage myoblasts, thereby integrating bioenergetics, redox balance, and cell behavior within a unified experimental framework. In doing so, this work addresses current interpretability gaps in PBM research and provides new mechanistic insight into how light source, wavelength, and cellular age shape mitochondrial and functional responses in skeletal muscle cells.

2. Results

2.1. Effects of PBM on Mitochondrial Membrane Potential and ROS at the Single-Cell Level

To assess acute, source-specific mitochondrial and redox responses to photobiomodulation (PBM), single-cell measurements of mitochondrial membrane potential (ΔΨm, reported as MMP) and intracellular reactive oxygen species (ROS) were performed in C2C12 myoblasts at intermediate passage (P. 25) as an initial dose-response screen (Figure 1). ΔΨm and ROS were quantified using Rhodamine 123 (Rh123) and H_2DCFDA staining, respectively.

For MMP (ΔΨm), both 830 nm NIR laser and 660 nm LED irradiation produced significant, fluence-dependent increases in Rh123 fluorescence relative to baseline. The largest increase was observed at 5 J/cm², which was significantly higher than untreated controls and the 2.5 J/cm² condition ($p < 0.0001$), while 10 J/cm² did not further augment the response, consistent with a plateau in mitochondrial polarization (Figure 1A,B).

ROS levels also increased following PBM. For both light sources, 5 J/cm² elicited the most consistent elevation in H_2DCFDA signal relative to baseline, whereas 2.5 J/cm² did not differ from control conditions and 10 J/cm² did not produce an additional significant increase compared with controls in this single-cell readout (Figure 1C,D).

Together, these single-cell data identified 5 J/cm² as a leading candidate dose for downstream testing. To verify whether this apparent plateau extended to population-level outcomes and to better resolve potential biphasic behavior, a broader fluence range was subsequently evaluated in bulk cultures using CCK-8 viability assays (2.5, 5, 10, and 15 J/cm²), and the final working dose was selected based on the combined single-cell and bulk dose–response results.

2.2. Effects of PBM on Metabolic Activity, ATP Production, and ROS Signaling in Young and Replicatively Aged C2C12 Cells

To characterize population-level PBM responses and to guide fluence selection for downstream functional assays, metabolic activity was evaluated using the CCK-8 assay in young (≤5 passages) and replicatively aged (≥30 passages) C2C12 cells exposed to 660 nm LED or 830 nm NIR irradiation across fluences from 0 to 15 J/cm² (Figure 2A–C).

Under LED irradiation (Figure 2A), both young and aged cells exhibited significant increases in optical density (OD), consistent with enhanced metabolic viability following PBM exposure. A biphasic dose–response pattern was observed, with maximal enhancement at 5 J/cm² and attenuated responses at higher fluences. Across all tested doses, aged cells displayed significantly higher OD values than young cells, indicating greater metabolic responsiveness to LED-based PBM in the replicatively aged population.

© 2025 by the author(s). Distributed under a Creative Commons CC BY license.

Preprints.org (www.preprints.org) | NOT PEER-REVIEWED | Posted: 5 February 2026 doi:10.20944/preprints202602.0413.v1

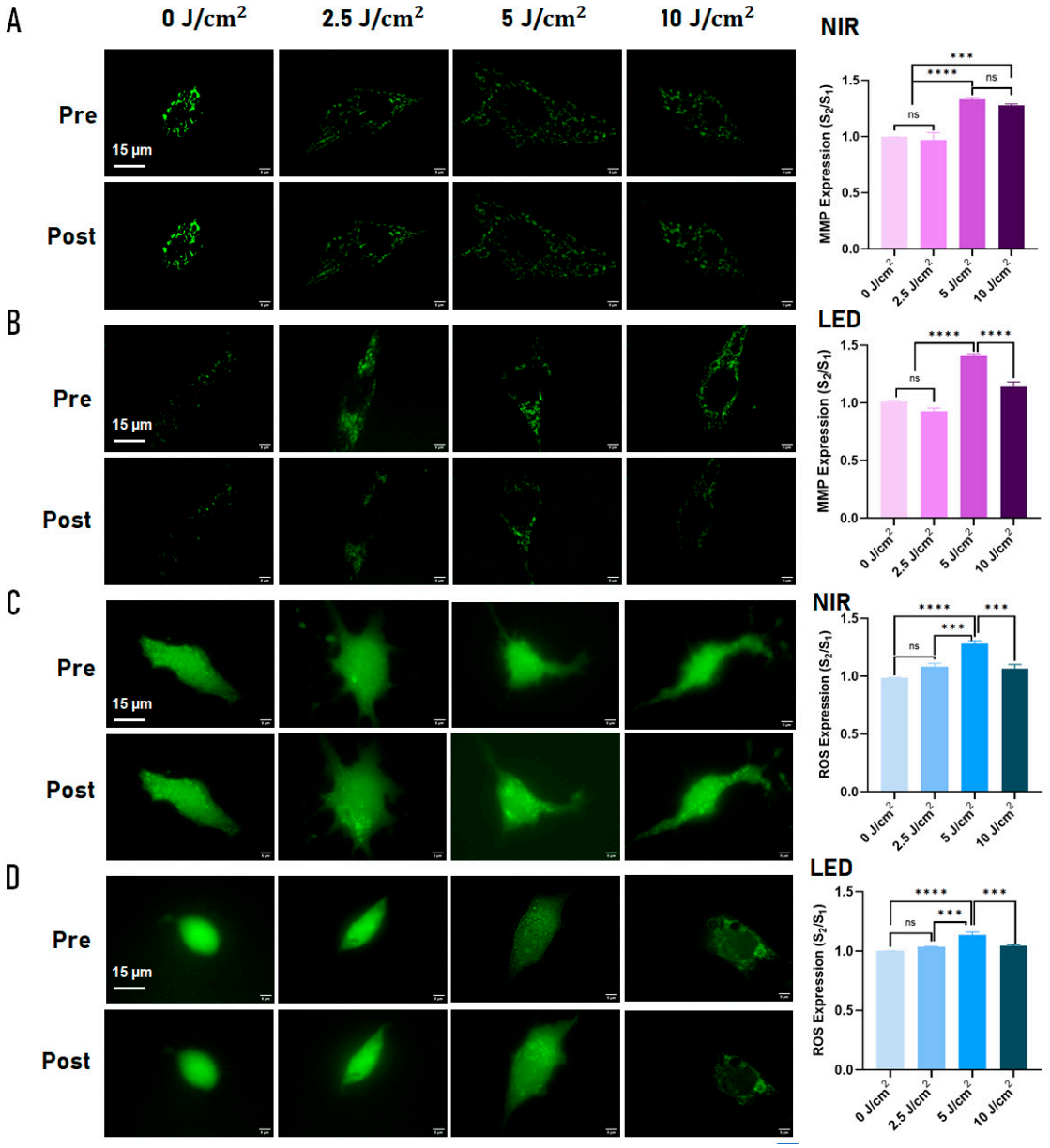

Figure 1. Source- and fluence-dependent modulation of mitochondrial membrane potential (ΔΨm, MMP) and reactive oxygen species (ROS) at the single-cell level following photobiomodulation (PBM) in mid-passage C2C12 myoblasts (P25). (A) Rhodamine 123 (Rh123) fluorescence images of individual C2C12 cells acquired before (Pre) and after (Post) irradiation with an 830 nm near-infrared (NIR) laser at fluences of 0, 2.5, 5, and 10 J/cm², reflecting changes in mitochondrial membrane potential (ΔΨm, expressed as MMP). (B) Corresponding Rh123 fluorescence images following 660 nm LED irradiation under identical fluence conditions. For each condition, the same cells were imaged before and after PBM within the illuminated microchamber field. (C) H_2DCFDA fluorescence images showing intracellular ROS levels before and after NIR irradiation across the same fluence range. (D) H_2DCFDA fluorescence images following LED irradiation. Quantitative analysis of normalized fluorescence intensity ratios (post/pre, S_2/S_1) is shown in the right panels. Both NIR and LED irradiation induced significant, fluence-dependent increases in MMP and ROS, with maximal responses observed at 5 J/cm² and no further enhancement at 10 J/cm². Data are presented as mean ± SEM from ≥3 independent experiments. Statistical comparisons were performed using one-way ANOVA followed by Tukey's post hoc test; ns, not significant; ** $p < 0.01$; *** $p < 0.001$; **** $p < 0.0001$. Scale bars: 15 µm.

© 2025 by the author(s). Distributed under a Creative Commons CC BY license.

Preprints.org (www.preprints.org) | NOT PEER-REVIEWED | Posted: 5 February 2026 doi:10.20944/preprints202602.0413.v1

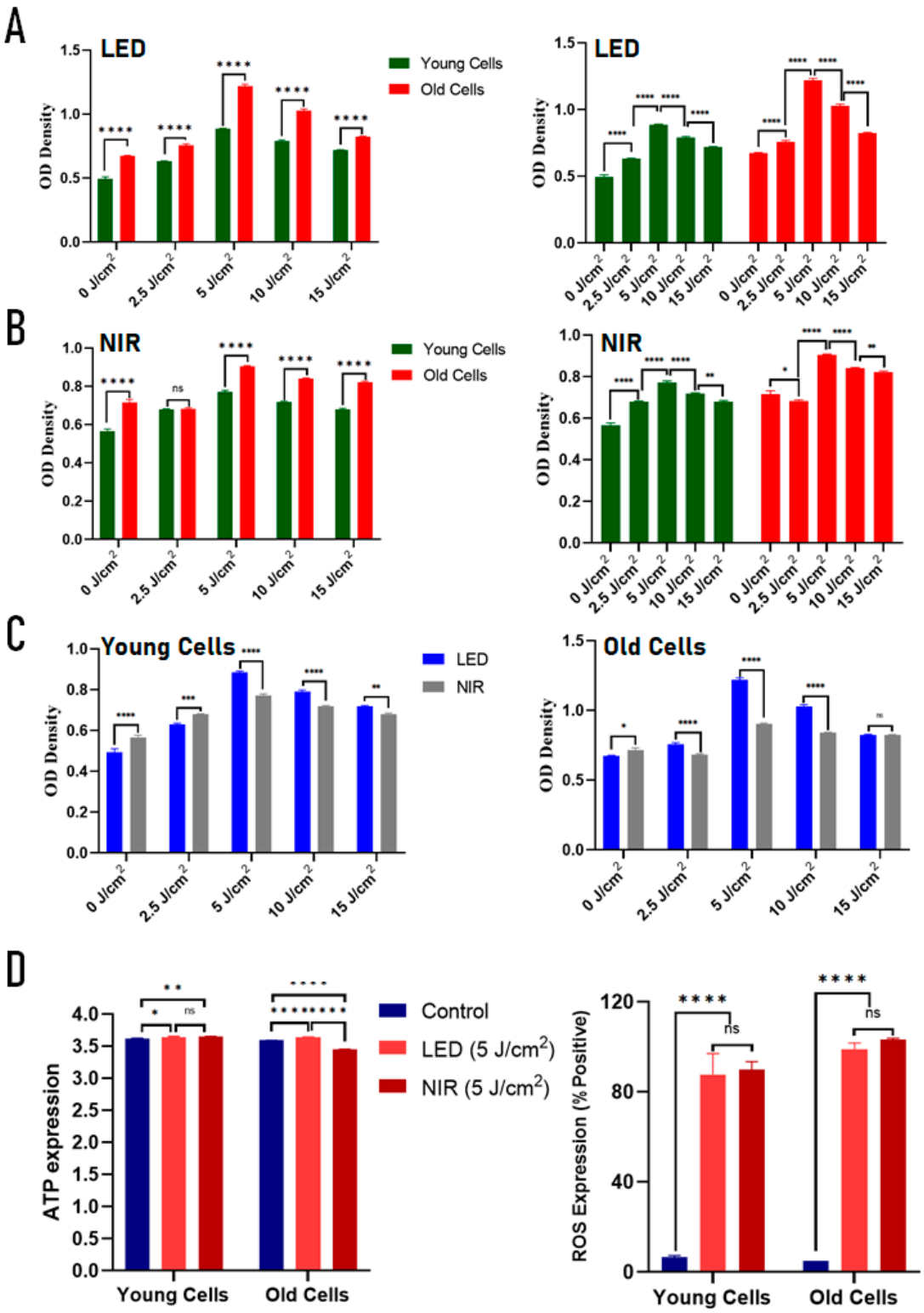

Figure 2. Photobiomodulation (PBM) enhances metabolic activity, ATP production, and redox signaling in young and replicatively aged C2C12 cells in a dose- and source-dependent manner. (A) CCK-8 assay showing optical density (OD) as an index of metabolic viability in young (≤5 passages, green) and old (≥30 passages, red) cells following 660 nm LED irradiation at fluences of 0, 2.5, 5, 10, and 15 J/cm². (B) CCK-8 assay showing OD in young and old cells following 830 nm NIR laser irradiation at the same fluences. Both irradiation sources produced biphasic dose–response patterns with maximal metabolic enhancement at 5 J/cm², followed by plateau or decline at higher fluences. Aged cells exhibited equal or greater metabolic responses compared with young cells, particularly under LED irradiation. (C) Direct comparison of LED (blue) and NIR (gray) effects on metabolic activity in young (left) and old (right) cells across fluences, demonstrating higher responses to LED at

© 2025 by the author(s). Distributed under a Creative Commons CC BY license.

Preprints.org (www.preprints.org) | NOT PEER-REVIEWED | Posted: 5 February 2026 doi:10.20944/preprints202602.0413.v1

several doses, especially at the optimal fluence of 5 J/cm². (D) ATP production (left) and intracellular ROS positivity (right) measured after PBM at 5 J/cm². Both LED and NIR significantly increased ATP levels and ROS signaling relative to controls in both young and old cells, with no significant differences between light sources at this dose. Data are presented as mean ± SEM from ≥3 independent experiments. Statistical comparisons were performed using one-way ANOVA followed by Tukey's post hoc test; **** $p < 0.0001$, *** $p < 0.001$, ** $p < 0.01$, * $p < 0.05$, ns = not significant.

Similarly, NIR irradiation induced significant increases in metabolic activity in both age groups (Figure 2B), again demonstrating a biphasic response with peak effects at 5 J/cm². In aged cells, the metabolic response at 5 J/cm² exceeded that observed in young cells, suggesting that PBM sensitivity to NIR is preserved, and in some conditions enhanced, despite replicative aging.

Direct comparison of light sources (Figure 2C) revealed that LED irradiation produced greater metabolic enhancement than NIR at several fluences in both young and aged cells, with the largest source-dependent differences observed at the optimal dose of 5 J/cm². These findings indicate that, beyond wavelength alone, source-specific delivery characteristics may influence PBM efficacy, particularly in metabolically compromised cellular states.

Based on the concordant identification of 5 J/cm² as the optimal fluence in both single-cell mitochondrial assays (Figure 1) and bulk metabolic screening, this dose was selected for subsequent mechanistic and functional analyses.

At 5 J/cm² (Figure 2D, left), ATP levels were significantly increased following PBM in both young and aged cells. In young cells, LED and NIR induced comparable ATP elevations, whereas in aged cells, LED produced a significantly greater increase in ATP compared with NIR, indicating age-dependent divergence in source-specific bioenergetic responsiveness.

Bulk ROS measurements at 5 J/cm² (Figure 2D, right) revealed marked increases in ROS-positive cells in both young and aged populations following PBM, with no significant difference between light sources within each age group. These elevations were consistent with controlled redox signaling rather than overt oxidative stress, supporting a mitohormetic contribution to PBM-mediated metabolic activation.

2.3. Extracellular Vesicle Release and Characterization Following PBM

Nanoparticle tracking analysis (NTA) was used to quantify extracellular vesicle (EV) release from early-passage (≤5) and late-passage (≥30) C2C12 myoblasts following photobiomodulation at 5 J/cm² using either 660 nm LED or 830 nm NIR irradiation. Representative size distributions revealed vesicle populations predominantly within the 50 to 200 nm range across all experimental conditions (Figure 3A).

Both light sources significantly increased EV particle counts relative to non-irradiated controls in young and old cells (Figure 3B, $p < 0.001$). In early-passage cells, NIR irradiation induced the highest EV yield, whereas in late-passage cells, LED treatment resulted in a comparatively greater increase in EV particle counts than NIR exposure, indicating an age-dependent shift in photonic source sensitivity.

To further assess qualitative differences in vesicle subpopulations, surface tetraspanin profiling was performed on EVs derived from young cells, which display higher metabolic and secretory activity and therefore provide a sensitive system for detecting source-specific differences in EV biogenesis. ExoView analysis confirmed the presence of canonical EV markers CD9, CD63, and CD81, while negative controls showed no detectable signal (Figure 3C).

Quantitative ExoView analysis revealed increased CD9- and CD81-positive particle counts following both LED and NIR treatments with NIR irradiation producing a higher proportion of triple-positive CD63/CD81/CD9 vesicles (Figure 3D,E). These findings indicate that, in metabolically active myoblasts, NIR-based PBM preferentially enhances the release of canonical small EV populations.

© 2025 by the author(s). Distributed under a Creative Commons CC BY license.

Preprints.org (www.preprints.org) | NOT PEER-REVIEWED | Posted: 5 February 2026 doi:10.20944/preprints202602.0413.v1

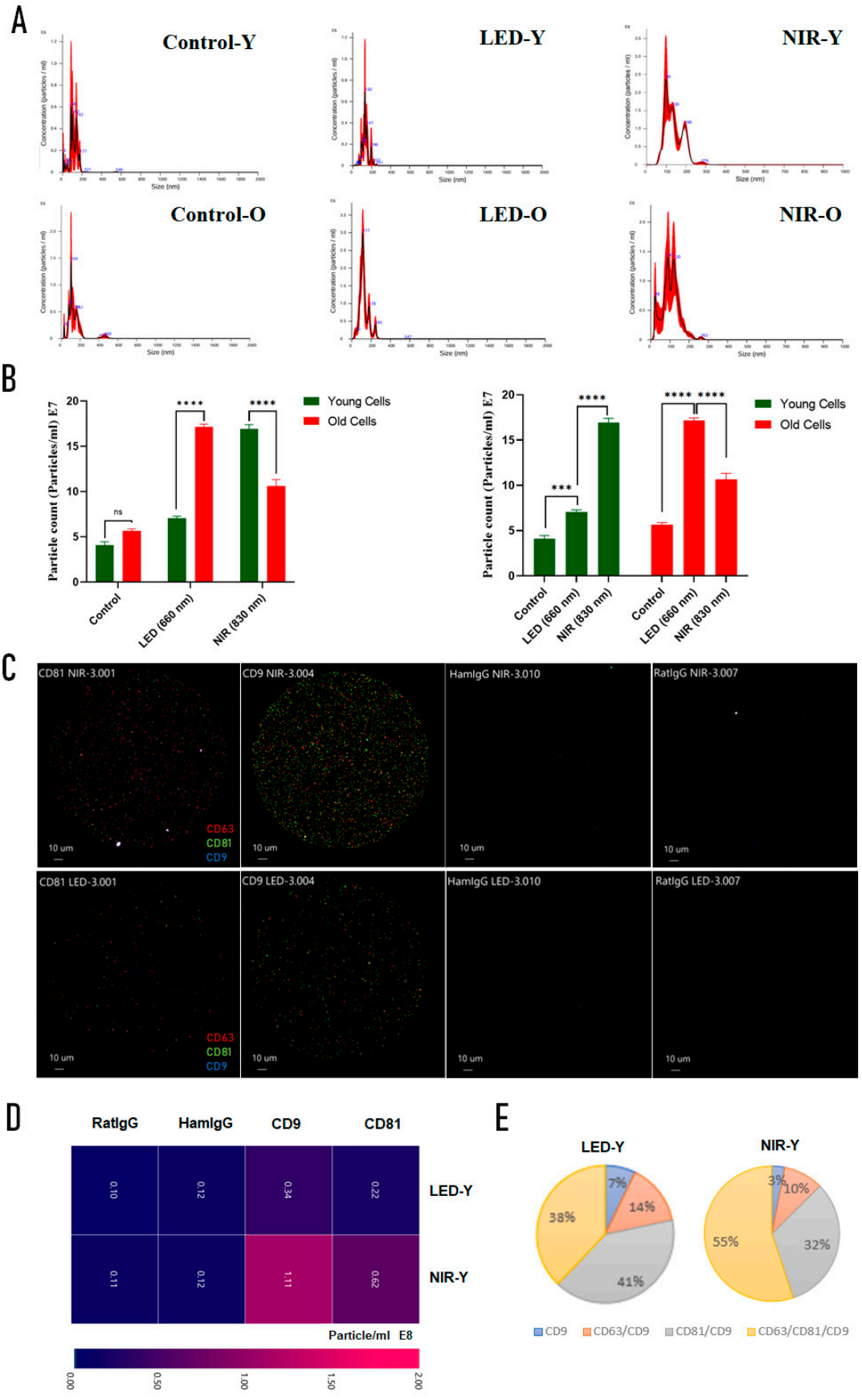

Figure 3. Source- and replicative stage-dependent regulation of extracellular vesicle (EV) release and subtype composition following photobiomodulation in C2C12 myoblasts. (A) Representative nanoparticle tracking

© 2025 by the author(s). Distributed under a Creative Commons CC BY license.

Preprints.org (www.preprints.org) | NOT PEER-REVIEWED | Posted: 5 February 2026 doi:10.20944/preprints202602.0413.v1

analysis (NTA) size distribution profiles of EVs isolated from control, LED-treated (660 nm), and NIR-treated (830 nm) C2C12 myoblasts at early passage (young, ≤5 passages) and late passage (old, ≥30 passages) following irradiation at 5 J/cm², showing vesicle populations predominantly within the 50–200 nm size range. (B) Quantification of EV particle concentration (particles/mL, $\times 10^7$) demonstrates significant PBM-induced increases in EV release in both young and old cells. NIR irradiation produced the greatest increase in EV secretion in young cells, whereas LED treatment induced a comparatively larger increase in EV particle counts in old cells, indicating age-dependent differences in source responsiveness. (C) Representative ExoView fluorescence micrographs of EVs isolated from young cells and captured using antibodies against CD9 and CD81, with co-detection of CD63 confirming canonical tetraspanin-positive EV populations. Negative controls using rat IgG and hamster IgG showed no detectable signal. Scale bar = 10 μm. (D) Heatmap showing relative abundance of CD9- and CD81-positive EV subpopulations (particles/mL, $\times 10^8$) in young cells following LED and NIR treatment, indicating increased canonical EV capture after PBM, with higher counts following NIR exposure. (E) Proportional distribution of EV subtypes in young cells expressed as a percentage of total detected particles, including CD9 single-positive, CD63/CD9, CD81/CD9, and triple-positive CD63/CD81/CD9 vesicles. NIR treatment increased the proportion of triple-positive canonical EVs compared with LED, suggesting enhanced organization or maturation of small EV populations under NIR stimulation. Data are presented as mean ± SEM from at least three independent experiments. Statistical significance is indicated as *$p < 0.05$, **$p < 0.01$, ***$p < 0.001$, ****$p < 0.0001$; ns, not significant.

2.4. Effects of PBM on Migration and Differentiation of Young and Old C2C12 Cells

Cell migration was evaluated using the wound-healing assay in young (≤5 passages) and old (≥30 passages) C2C12 myoblasts following PBM with LED (660 nm, 5 J/cm²) or NIR (830 nm, 5 J/cm²). Representative bright-field images at 36 h post-treatment illustrate the extent of gap closure in each condition (Figure 4A). Relative gap (%) was plotted over time, where lower values indicate greater wound closure (Figure 4B).

In both age groups, relative gap values increased at 12 h compared with baseline, indicating transient gap widening following insert removal and serum-free conditions immediately after PBM. From 16 h onward, progressive gap closure was observed across all conditions. In young cells, LED-treated cultures exhibited smaller relative gap values than controls at 24 h and significantly reduced gaps at 36 h, whereas NIR-treated cells showed delayed closure at 24 h followed by partial improvement at 36 h, but did not surpass LED-treated cultures in closure efficiency.

In old cells, LED-treated cultures showed improved closure relative to controls at 16 h; however, at later time points (24 h and 36 h), control cultures exhibited the smallest remaining gaps, while both LED- and NIR-treated groups showed delayed closure. NIR-treated old cells consistently exhibited larger residual gaps than controls across all post-12 h time points.

Interval-specific closure analysis revealed that the most rapid migration occurred between 12–16 h in both young and old cells, followed by a gradual decline in closure rate during subsequent intervals. In young cells, NIR showed slightly higher closure rates during the early post-widening phase (12–16 h), whereas LED promoted greater closure during the mid-phase of migration (16–24 h). In old cells, both PBM modalities showed transient increases in early interval closure rates, but these effects were not sustained and did not translate into improved overall wound closure compared with controls at later stages.

Together, these findings indicate that PBM induces time-dependent and age-dependent modulation of migration dynamics, with modest and transient effects that are more evident in young cells treated with LED, while sustained enhancement of wound closure in aged myoblasts was not observed under the present experimental conditions.

Differentiation capacity was assessed by calculating the fusion index, defined as the proportion of nuclei incorporated into multinucleated myotubes. Representative images combining bright-field visualization with Hoechst-stained nuclei (Figure 4C) revealed increased multinucleation in PBM-treated groups compared with controls, with the most prominent effect observed under NIR irradiation in both young and old cells.

© 2025 by the author(s). Distributed under a Creative Commons CC BY license.

Preprints.org (www.preprints.org) | NOT PEER-REVIEWED | Posted: 5 February 2026 doi:10.20944/preprints202602.0413.v1

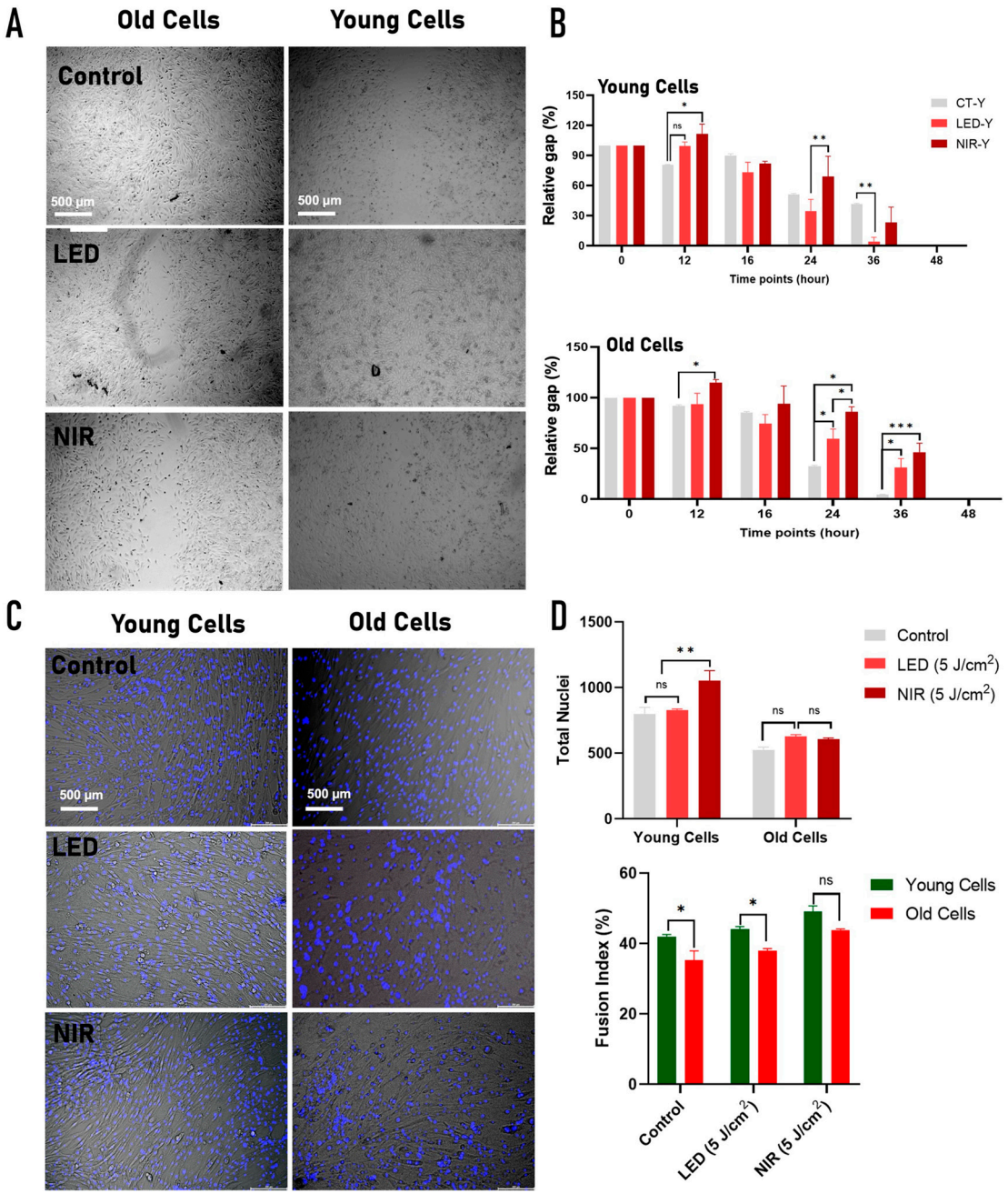

Figure 4. Effects of photobiomodulation on migration and myogenic differentiation in young and replicatively aged C2C12 myoblasts. (A) Representative bright-field images of wound-healing assays in early-passage (young, ≤5) and late-passage (old, ≥30) C2C12 cells under control, LED (660 nm, 5 J/cm²), and NIR (830 nm, 5 J/cm²) conditions. Images were acquired 36 h after scratch induction. Scale bars: 500 µm. (B) Quantification of relative wound gap area over time (0–48 h), normalized to the initial gap (100%). A transient increase in gap width at 12 h was observed across groups, indicative of cell retraction following medium replacement with serum-free conditions. Modest enhancement of gap closure was observed in young cells treated with LED at later time points (16, 34, 36 h), whereas no consistent acceleration of migration was detected in old cells under either PBM condition compared with controls. (C) Representative images of differentiated myotubes stained with Hoechst 33342 (blue) showing nuclear incorporation into multinucleated fibers in young and old cells following control, LED, or NIR treatment. Scale bars: 500 µm. (D) Quantification of total nuclei (upper panel) and fusion index (lower panel). NIR irradiation significantly increased total nuclei in young cells, while no significant differences in nuclei counts were observed among treatments in old cells. Fusion index analysis demonstrated significantly lower myogenic fusion in old compared with young cells under control and LED

© 2025 by the author(s). Distributed under a Creative Commons CC BY license.

Preprints.org (www.preprints.org) | NOT PEER-REVIEWED | Posted: 5 February 2026 doi:10.20944/preprints202602.0413.v1

conditions. Notably, NIR treatment eliminated the statistical difference between young and old groups, indicating partial restoration of differentiation capacity in replicatively aged myoblasts. Data are presented as mean ± SEM from three independent experiments. Statistical analysis was performed using one-way or two-way ANOVA with Tukey's post hoc test as appropriate. *p < 0.05, **p < 0.01, ***p < 0.001; ns, not significant.

Quantification of total nuclei per field in the case of NIR treatment significantly increased total nuclei in young cells but not in old cells (Figure 4D, upper panel)., consistent with a modest age-dependent response under differentiation-inducing conditions. Overall, nuclei counts remained within a similar range across treatments, reflecting near-confluent cultures maintained in low-serum medium to favor differentiation over proliferation.

In contrast, fusion index analysis demonstrated marked age- and treatment-dependent effects (Figure 4D, lower panel). In old cells, the fusion index increased from 35.2 ± 4.7% in controls to 38.0 ± 1.1% with LED and 43.9 ± 0.5% with NIR. Statistical comparisons showed a significant improvement with NIR versus control ($p = 0.033$) and a highly significant increase with NIR versus LED ($p < 0.001$), whereas LED alone did not significantly differ from control ($p = 0.377$).

In young cells, the fusion index increased from 42.0 ± 1.0% in controls to 44.1 ± 1.3% with LED and 49.1 ± 2.8% with NIR. NIR significantly enhanced fusion relative to both control ($p = 0.014$) and LED ($p = 0.047$), while LED treatment alone showed only a nonsignificant trend toward improvement compared with control ($p = 0.094$).

Together, these data indicate that PBM, particularly NIR irradiation, robustly enhances myogenic fusion in both young and aged C2C12 myoblasts, whereas effects on total cell number are minimal or age-dependent under differentiation-inducing conditions.

2.5. Integrated Summary of PBM Responses Across Cellular Outputs

To provide an integrated overview of PBM responses across biological scales, the principal outcomes of single-cell, population-level, and functional assays are summarized in Tables 1 and 2. At the single-cell level (passage 25), both LED and NIR irradiation produced fluence-dependent increases in mitochondrial membrane potential and moderate ROS signaling, with maximal responses observed at 5 J/cm², which, in combination with the cell viability test, guided dose selection for subsequent experiments. No major source-dependent differences were detected in these acute mitochondrial and redox responses.

At the population and functional levels, source- and age-dependent divergence became evident. LED irradiation consistently induced stronger metabolic activation and ATP production, particularly in replicatively aged cells. Both LED and NIR significantly increased extracellular vesicle release in young and aged cells, with NIR producing the highest EV yield in young cells, whereas aged cells exhibited a greater EV release response to LED. In young cells, NIR additionally enriched canonical EV subpopulations, suggesting enhanced biogenesis of small EV fractions. Migration responses were modest, transient, and highly phase-dependent, with no sustained enhancement of wound closure observed in aged myoblasts under either light source.

In contrast, myogenic differentiation was robustly enhanced by NIR irradiation in both young and aged cells, as reflected by significant increases in fusion index, whereas LED produced only mild or nonsignificant effects on fusion. Together, these findings indicate that although LED and NIR similarly activate mitochondrial and redox signaling at the single-cell level, they diverge at higher-order biological outputs. LED preferentially supports metabolic activation, particularly in aged cells, whereas NIR preferentially promotes myogenic differentiation and EV-associated paracrine signaling, with these functional distinctions becoming more pronounced in the context of cellular aging.

© 2025 by the author(s). Distributed under a Creative Commons CC BY license.

Preprints.org (www.preprints.org) | NOT PEER-REVIEWED | Posted: 5 February 2026 doi:10.20944/preprints202602.0413.v1

Table 1. Summary of Single-Cell PBM Responses and Dose Selection (C2C12, Passage 25). Purpose: Acute mitochondrial and redox sensing to identify optimal fluence.

Output (Single-cell)	LED (660 nm)	NIR (830 nm)	Dose Dependence / Interpretation
Mitochondrial membrane potential (ΔΨm, Rh123)	↑ at 5 J/cm²	↑ at 5 J/cm²	Biphasic, plateau ≥10 J/cm² — Both sources enhance mitochondrial polarization; optimal response at 5 J/cm²
Intracellular ROS (H_2DCFDA)	↑ at 5 J/cm²	↑ at 5 J/cm²	Biphasic — Moderate ROS signaling consistent with mitohormetic activation
Source comparison	Comparable to NIR	Comparable to LED	No strong wavelength-specific differences at single-cell level
Dose selection outcome	5 J/cm² selected	5 J/cm² selected	Guided dose for population-level assays

↑ increase relative to baseline.

Table 2. Summary of Population-Level and Functional PBM Effects by Age and Light Source. Purpose: Biological outcomes under optimal fluence (5 J/cm²).

Output / Assay	Young Cells LED (660 nm)	Young Cells NIR (830 nm)	Old Cells LED (660 nm)	Old Cells NIR (830 nm)	Key Biological Trend
Metabolic activity (CCK-8)	↑↑	↑	↑↑	↑	LED produces stronger metabolic activation
ATP production	↑ (≈ NIR)	↑ (≈ LED)	↑↑ (LED > NIR)	↓	Aged cells show greater ATP response to LED
Bulk ROS (% positive cells)	↑↑	↑↑	↑↑	↑↑	Strong redox activation independent of irradiation modality
EV particle release (NTA) [Phenotype in early-passage]	↑ [↑ CD9/CD81]	↑↑ [↑↑ triple-positive EVs]	↑↑	↑	Source sensitivity shifts with age [NIR favors canonical small EV populations]
Migration (wound healing)	↑↑ sustained (24–36 h)	↑ transient / delayed	↑ early only (16 h)	No sustained effect	Migration weak and strongly age-dependent; LED modestly improves young cell closure
Myogenic fusion (fusion index)	Trend ↑	Significant ↑↑	NS	Significant ↑↑	NIR strongly promotes differentiation

↑ modest increase; ↑↑ strong increase; ↓ decrease relative to control; NS not significant.

3. Discussion

3.1. Dose-Dependent Mitochondrial Responses to PBM

Our results confirm that PBM produces dose-dependent effects on mitochondrial function, with 5 J/cm² consistently emerging as the optimal fluence for enhancing viability, ATP production, and mitochondrial membrane potential. Transient increases in ΔΨm and ROS at the single-cell level align with the photoreceptor model in which photons at 660–830 nm interact with cytochrome c oxidase to enhance electron transport and proton pumping, briefly elevating membrane potential and producing signaling ROS [3,35–37]. These pulses fit the framework of mitohormesis, where moderate, short-lived ROS act as second messengers that help coordinate adaptive transcriptional and metabolic programs rather than causing damage [7,8,37]. The biphasic profile we observed is

© 2025 by the author(s). Distributed under a Creative Commons CC BY license.

Preprints.org (www.preprints.org) | NOT PEER-REVIEWED | Posted: 5 February 2026 doi:10.20944/preprints202602.0413.v1

consistent with classic PBM literature showing that low-to-moderate doses trigger pro-survival signaling while higher exposures plateau or reverse benefits [15,38].

Methodologically, our single-cell ΔΨm tracking with Rh123 is supported by bioenergetics literature that validates cationic probes for dynamic ΔΨm readouts when imaging parameters are controlled [39–41]. While both single-cell imaging and bulk population assays revealed significant ROS elevations following PBM, neither approach resolved wavelength-dependent differences, indicating that mitochondrial redox activation is robust but largely source-independent, and that functional divergence likely emerges from downstream signaling, subcellular distribution, or cumulative metabolic integration rather than acute ROS magnitude [7,35,38].

3.2. Age-Dependent Differences in Mitochondrial and Redox Responses

A major aim of this work was to determine whether photobiomodulation produces age-specific mitochondrial and redox responses. Comparing young (≤5 passages) and replicatively aged (≥30 passages) C2C12 myoblasts revealed that cellular age shapes PBM responsiveness. In young cells, PBM increased ATP and markedly elevated the proportion of ROS-positive cells, with both LED and NIR producing significant redox activation. In old cells, PBM also robustly increased bulk ROS, but ATP responses diverged in a modality-dependent manner, with LED producing a strong energetic increase while NIR resulted in a significant reduction in ATP. This pattern is consistent with aging literature describing altered redox set points, reduced adaptive plasticity, and persistent deficits in mitochondrial efficiency that can uncouple redox signaling from downstream energetic gain in aged systems [21–23]. Mechanistically, PBM is proposed to modulate electron transport through CcO, including potential displacement of inhibitory nitric oxide at complex IV, but the direction and efficiency of energy conversion may depend on the aged mitochondrial context and delivery characteristics of each modality [2,5,6]. The combined observation of strong ROS induction alongside bidirectional ATP outcomes in old cells supports a hormetic framework in which redox activation can be preserved, yet energetic benefit is constrained or redirected depending on the cellular state and PBM modality [7,8,37].

The use of low- and high-passage C2C12 myoblasts reflects a replicative aging model that is widely employed to study mitochondrial decline, impaired differentiation, altered redox balance, and metabolic inflexibility. High-passage C2C12 cells exhibit documented deficits in proliferation, fusion, antioxidant regulation, and mitochondrial function, making this system suitable for probing age-sensitive photobiomodulation responses. [33,34,42] Although molecular markers of cellular senescence were not assessed in the present study, the consistent passage-dependent patterns observed across bioenergetic, redox, functional, and extracellular vesicle-related endpoints support the biological relevance of this aging-associated model for investigating PBM-induced mitochondrial and myogenic modulation.

3.3. Functional Outcomes: Migration and Differentiation

Quantitative analysis of wound closure revealed that PBM modulated migration dynamics in a time-dependent and age-dependent manner, but did not produce sustained enhancement of wound closure, particularly in replicatively aged C2C12 myoblasts. In young cells, NIR treatment was associated with slightly higher closure rates during the early post-widening phase (12–16 h), whereas LED promoted greater gap reduction during the mid-phase of migration (16–24 h), leading to significantly smaller residual gaps at 36 h compared with both control and NIR-treated groups. In aged cells, although both PBM modalities transiently increased early closure rates, control cultures exhibited the smallest remaining gaps at later time points, while LED- and NIR-treated groups showed delayed closure. These findings indicate that PBM influences migration kinetics primarily during early and mid phases, but does not confer durable improvement in wound closure in aged myoblasts.

Compared with our previous findings in human adipose-derived stem cells (hADSCs), where NIR irradiation at 5 J/cm² robustly enhanced migration in a biphasic dose-dependent manner [38],

© 2025 by the author(s). Distributed under a Creative Commons CC BY license.

Preprints.org (www.preprints.org) | NOT PEER-REVIEWED | Posted: 5 February 2026 doi:10.20944/preprints202602.0413.v1

C2C12 myoblasts in the present study exhibited only modest and transient migration responses to PBM. This discrepancy likely reflects intrinsic lineage-specific functional priorities. Mesenchymal stem cells rely heavily on motility for tissue homing and repair, whereas myoblasts, once near confluence, shift toward fusion-driven differentiation programs rather than continued migration. Under differentiation-permissive conditions, cellular energy and signaling resources may therefore be preferentially allocated to myotube formation rather than wound closure, explaining the limited migratory enhancement observed despite clear mitochondrial and metabolic activation.

By contrast, myogenic differentiation was robustly enhanced by NIR irradiation at 5 J/cm² in both young and aged cells, as reflected by significant increases in fusion index. In aged cells, NIR treatment increased fusion to levels that were no longer significantly different from those observed in young cells, indicating partial functional rescue of age-associated differentiation deficits. In young cells, NIR also produced significantly greater fusion compared with both control and LED-treated groups, whereas LED alone resulted only in modest and statistically nonsignificant improvements. A higher fusion index is consistent with a model in which improved $\Delta\Psi m$ and ATP availability support cytoskeletal remodeling and myogenic transcriptional programs required for fusion [18,43,44]. Transient ROS can activate pro-myogenic pathways, including NF-κB and MAPK signaling, when kept within a physiological range, whereas persistent oxidative stress impairs differentiation and promotes apoptotic signaling that blocks myogenesis [24,34,45,46]. The selective improvement of differentiation under NIR in both age groups aligns with a bioenergetics-first mechanism that supplies ATP while maintaining ROS within signaling bounds rather than entering a damage regime [21,34].

In parallel, quantification of total nuclei per field revealed age- and treatment-dependent differences. In young cells, NIR significantly increased total nuclei compared with both control and LED-treated groups, suggesting enhanced cell survival or retention under differentiation conditions. In aged cells, total nuclei did not differ significantly across treatments, indicating limited proliferative or survival responsiveness in the context of replicative aging and serum-restricted differentiation. These findings likely reflect the experimental design, in which cells were induced to differentiate at near-confluent density and proliferation was restricted by serum withdrawal. Under such conditions, increases in fusion index more directly reflect differentiation efficiency instead of changes in cell number, supporting the conclusion that NIR preferentially enhances myogenic maturation over proliferation.

Together, these functional data demonstrate that while PBM exerts modest and transient effects on migration, particularly in young cells, NIR irradiation at 5 J/cm² consistently promotes myogenic differentiation across age groups and partially mitigates age-associated impairments in fusion capacity. This dissociation between migratory and differentiation responses suggests that PBM preferentially supports later-stage myogenic programs rather than early motility-driven processes in replicatively aged muscle progenitors.

3.4. PBM-Induced Extracellular Vesicle Release

NTA quantification was performed in EV preparations from both early- and late-passage cells, whereas single-particle tetraspanin phenotyping (ExoView) was performed in early-passage EVs to resolve source-dependent differences in canonical marker co-expression.

Photobiomodulation significantly enhanced extracellular vesicle release, with source- and age-dependent differences in both particle yield and vesicle composition. EV biogenesis is tightly linked to mitochondrial bioenergetics, intracellular calcium dynamics, and redox signaling, all of which are known targets of PBM. Activation of these pathways can promote vesicle formation through both (Endosomal Sorting Complex required for Transport) ESCRT-dependent and tetraspanin-enriched mechanisms. [38,47].

In early-passage myoblasts, NIR irradiation produced the greatest increase in EV secretion and was associated with a higher proportion of triple-positive CD63/CD81/CD9 vesicles, consistent with enhanced release of canonical small EV populations. This response aligns with robust PBM-induced

© 2025 by the author(s). Distributed under a Creative Commons CC BY license.

Preprints.org (www.preprints.org) | NOT PEER-REVIEWED | Posted: 5 February 2026 doi:10.20944/preprints202602.0413.v1

mitochondrial and redox activation at 5 J/cm², while ATP increases in young cells were comparable between LED and NIR, suggesting that EV biogenesis may be supported by coordinated mitochondrial polarization and signaling ROS rather than a uniquely greater ATP gain under NIR. Together, these findings support the concept that bioenergetic state and redox-regulated trafficking can facilitate vesicle biogenesis and cargo organization.

In contrast, late-passage cells exhibited a greater increase in EV particle counts following LED treatment compared with NIR. Replicative aging is associated with altered endosomal trafficking, membrane remodeling, and stress-responsive vesicle release, which may favor quantitatively increased but phenotypically distinct EV populations under different photonic stimuli. Whether these vesicles represent canonical exosomes or alternative vesicle subtypes remains to be determined.

Together, these findings indicate that photobiomodulation not only regulates EV release but that the dominant light source driving vesicle secretion shifts with cellular aging, reflecting age-dependent constraints on mitochondrial signaling and vesicle biogenesis pathways. This suggests that PBM may influence both direct cellular responses and paracrine signaling networks in an age-specific manner, with potential implications for regenerative and anti-sarcopenic strategies. [48].

3.5. Wavelength and Source Considerations

Differences between 660 nm LED and 830 nm NIR irradiation likely reflect a combination of optical and biochemical factors. Penetration depth and reduced scattering at near-infrared wavelengths favor 830 nm light for delivery through multilayered cellular systems and tissues, potentially enhancing effective photon availability at mitochondrial chromophores such as cytochrome c oxidase [25]. When irradiance and fluence are matched, both lasers and LEDs are capable of activating canonical PBM mechanisms; however, differences in spectral bandwidth, coherence, and beam homogeneity can influence the realized dose and spatial distribution of photons at the cellular level [30,49].

In the present study, calibration procedures were designed to equalize fluence at the culture plane for both light sources. Under these controlled conditions, LED and NIR produced comparable mitochondrial and redox activation at the single-cell level, but diverged at higher-order biological outputs. LED irradiation preferentially enhanced metabolic activity and ATP production, particularly in replicatively aged myoblasts, whereas NIR irradiation more consistently promoted myogenic differentiation and the release of canonical extracellular vesicle subpopulations. These findings suggest that source-, wavelength-dependent optical properties interact with cell-type- and age-specific metabolic constraints to bias PBM outcomes toward distinct functional programs, rather than conferring a uniform advantage to a single light source [13,18,50].

3.6. Translational Relevance for Age-Related Progressive Muscle Conditions

Age-related muscle decline is characterized by mitochondrial inefficiency, impaired myogenic differentiation, and dysregulated redox balance [21,22]. In this context, our findings demonstrate that photobiomodulation engages multiple mitochondrial- and redox-regulated pathways relevant to muscle aging, with distinct age- and wavelength-dependent outcomes. Notably, 830 nm NIR irradiation at moderate fluence robustly enhanced myogenic fusion in replicatively aged C2C12 myoblasts, partially restoring differentiation capacity toward levels observed in young cells. This improvement occurred despite minimal effects on migration kinetics and reflects a selective enhancement of late-stage myogenic programs that are particularly compromised with aging. These effects support the concept that PBM can activate adaptive, redox-dependent programs involved in muscle regeneration and cellular resilience. Prior preclinical and human studies have similarly reported improvements in mitochondrial function and muscle performance following PBM, particularly when combined with exercise-based interventions [13,14].

In parallel, photobiomodulation significantly increased extracellular vesicle release, although the dominant light source driving vesicle secretion shifted with cellular age. In young myoblasts, NIR preferentially enhanced EV output and enriched canonical small EV subpopulations, whereas in aged

© 2025 by the author(s). Distributed under a Creative Commons CC BY license.

Preprints.org (www.preprints.org) | NOT PEER-REVIEWED | Posted: 5 February 2026 doi:10.20944/preprints202602.0413.v1

cells, LED irradiation induced a greater increase in total EV particle counts. These findings suggest that age-associated constraints on mitochondrial signaling, membrane trafficking, and endosomal processing shape how photonic stimulation is translated into paracrine signaling outputs. Such EV-mediated effects may contribute to tissue-level adaptation and intercellular communication in aging muscle, even when direct migratory responses are limited.

While near-infrared wavelengths are often favored for their deeper tissue penetration in vivo [25,30], our in vitro findings indicate that functional outcomes are not determined by source alone. Under matched dosimetry, LED- and NIR-based photobiomodulation elicited comparable mitochondrial polarization and redox signaling at the single-cell level, yet diverged in their higher-order biological outcomes. These findings indicate that PBM effects are not determined by wavelength alone but are shaped by source-specific properties of light delivery, including coherence, spectral bandwidth, and spatial irradiance distribution. Accordingly, LED and NIR should not be regarded as interchangeable modalities but as complementary photonic sources with distinct biological emphases. LED irradiation preferentially supported metabolic activation and ATP production, particularly in replicatively aged cells, whereas NIR irradiation more consistently promoted myogenic differentiation across age groups. This source-specific divergence is consistent with prior evidence showing that both coherent and non-coherent light can activate mitochondrial photoacceptors when dosimetry is carefully controlled, while differing in how upstream mitochondrial signals are translated into functional cellular programs. [28,30].

Collectively, the present findings indicate that PBM can modulate bioenergetic, redox, and differentiation pathways that are central to age-associated impairments in muscle regeneration and cellular resilience. The observed age- and wavelength-dependent divergence between LED and NIR irradiation emphasizes the importance of tailoring PBM parameters to specific biological objectives, such as metabolic support, differentiation enhancement, or paracrine signaling. Nevertheless, extrapolation beyond cellular systems requires caution, as tissue architecture, vascularization, immune interactions, and systemic metabolic regulation are not captured in vitro [26]. Future in vivo and longitudinal studies will therefore be essential to determine whether the mitochondrial, redox, and myogenic adaptations identified here translate into sustained improvements in muscle function at the organismal level.

4. Materials and Methods

Figure 5 provides a schematic overview of the experimental design, illustrating the single-cell dose-screening strategy and the subsequent population-level and functional assays performed in young and replicatively aged C2C12 myoblasts. Detailed methods for each experimental step are described below.

4.1. Cell Culture

C2C12 murine myoblasts (ATCC® CRL-1772™) were kindly provided by Professor Yi-Fan Chen (College of Medical Science and Technology, Taipei Medical University) and Dr. Aline Yen-Ling Wang (Center for Vascularized Composite Allotransplantation, Chang Gung Memorial Hospital). Cells were cultured in Dulbecco's Modified Eagle Medium (DMEM, Gibco, Cat#11965-084) without sodium pyruvate, supplemented with 10% fetal bovine serum (FBS; Gibco) and 1% penicillin–streptomycin. Cultures were maintained at 37 °C in a humidified 5% CO_2 atmosphere. Cells were routinely passaged at 50–60% confluence to maintain a proliferative myoblastic phenotype and avoid spontaneous differentiation [34,51]. Young cells were defined as passage ≤5, while old cells were defined as passage ≥ 30, consistent with established models of replicative aging in myoblasts [18,33,34,43,52,53].

© 2025 by the author(s). Distributed under a Creative Commons CC BY license.

Preprints.org (www.preprints.org) | NOT PEER-REVIEWED | Posted: 5 February 2026 doi:10.20944/preprints202602.0413.v1

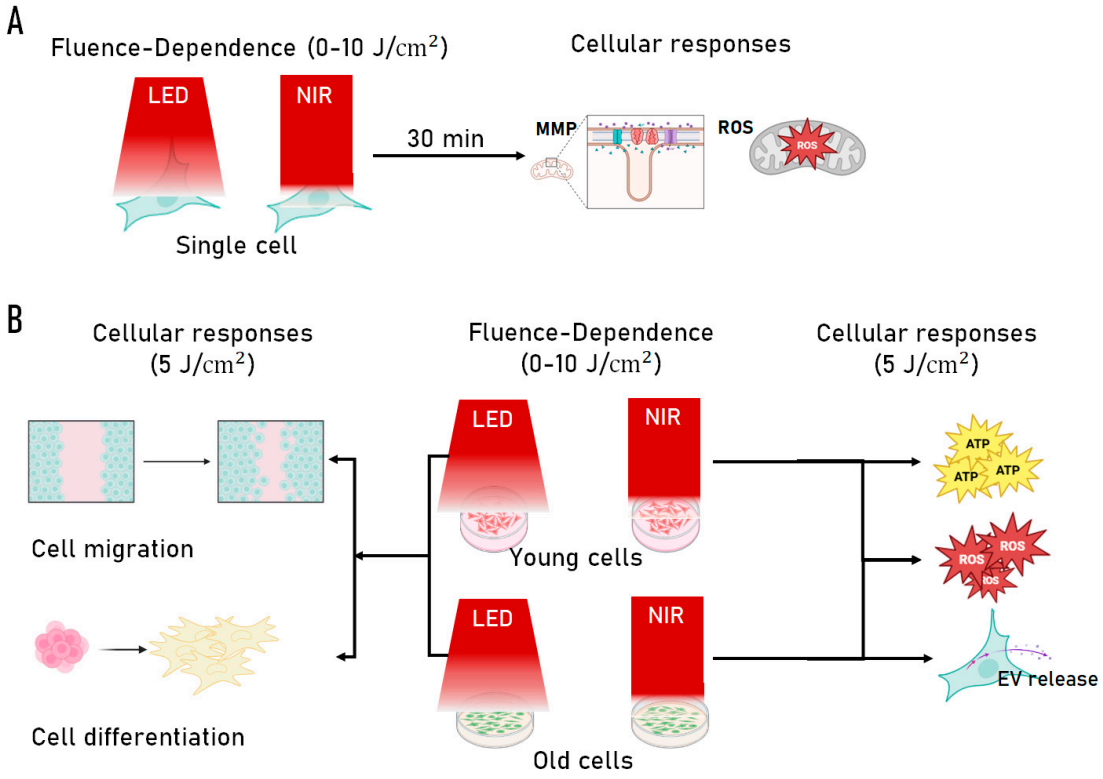

Figure 5. Roadmap of the photobiomodulation (PBM) experimental design. (A) Single-cell experimental workflow illustrating fluence-dependent PBM exposure (0–10 J/cm²) using either a 660 nm LED or an 830 nm NIR laser, followed by quantitative assessment of mitochondrial membrane potential (ΔΨm, reported as MMP) and reactive oxygen species (ROS) at the individual cell level (passage 25). (B) Population-level experimental design in which C2C12 myoblasts representing different replicative ages, defined as young (≤5 passages) and old (≥30 passages), were exposed to source-specific PBM across the same fluence range, with functional outcomes assessed at an optimized fluence (5 J/cm²), including ATP production, ROS levels, extracellular vesicle (EV) release, cell migration, and myogenic differentiation. Together, this roadmap summarizes the integrated strategy linking light source, fluence, and replicative cellular age to mitochondrial and regenerative responses.

Cryopreservation was performed in complete medium with 5% dimethyl sulfoxide (DMSO). Cells were stored in liquid nitrogen and thawed by rapid warming at 37 °C, followed by centrifugation at 200 × g for 5 min and resuspension in fresh medium. Differentiation was induced at 90% confluence by switching to DMEM supplemented with 2% horse serum (non-heat inactivated; Gibco Ref.16050-122) and refreshing medium daily. [54,55].

4.2. Photobiomodulation (PBM) Irradiation Systems

Three complementary PBM platforms were employed in this study (Figure 6), consisting of a near-infrared (NIR) laser source at 830 nm and a red light-emitting diode (LED) source at 660 nm, each configured for single-cell microchamber irradiation as well as for bulk population exposure in 96-well and 24-well plate formats.

For all systems, delivered fluence was calculated from the measured output power, exposure duration, and illuminated area using the standard relationship [59]:

$$\text{Fluence J/cm}^2 = \frac{\text{power (W)} \times \text{time (s)}}{\text{area (cm}^2\text{)}} \quad (1)$$

© 2025 by the author(s). Distributed under a Creative Commons CC BY license.

Preprints.org (www.preprints.org) | NOT PEER-REVIEWED | Posted: 5 February 2026 doi:10.20944/preprints202602.0413.v1

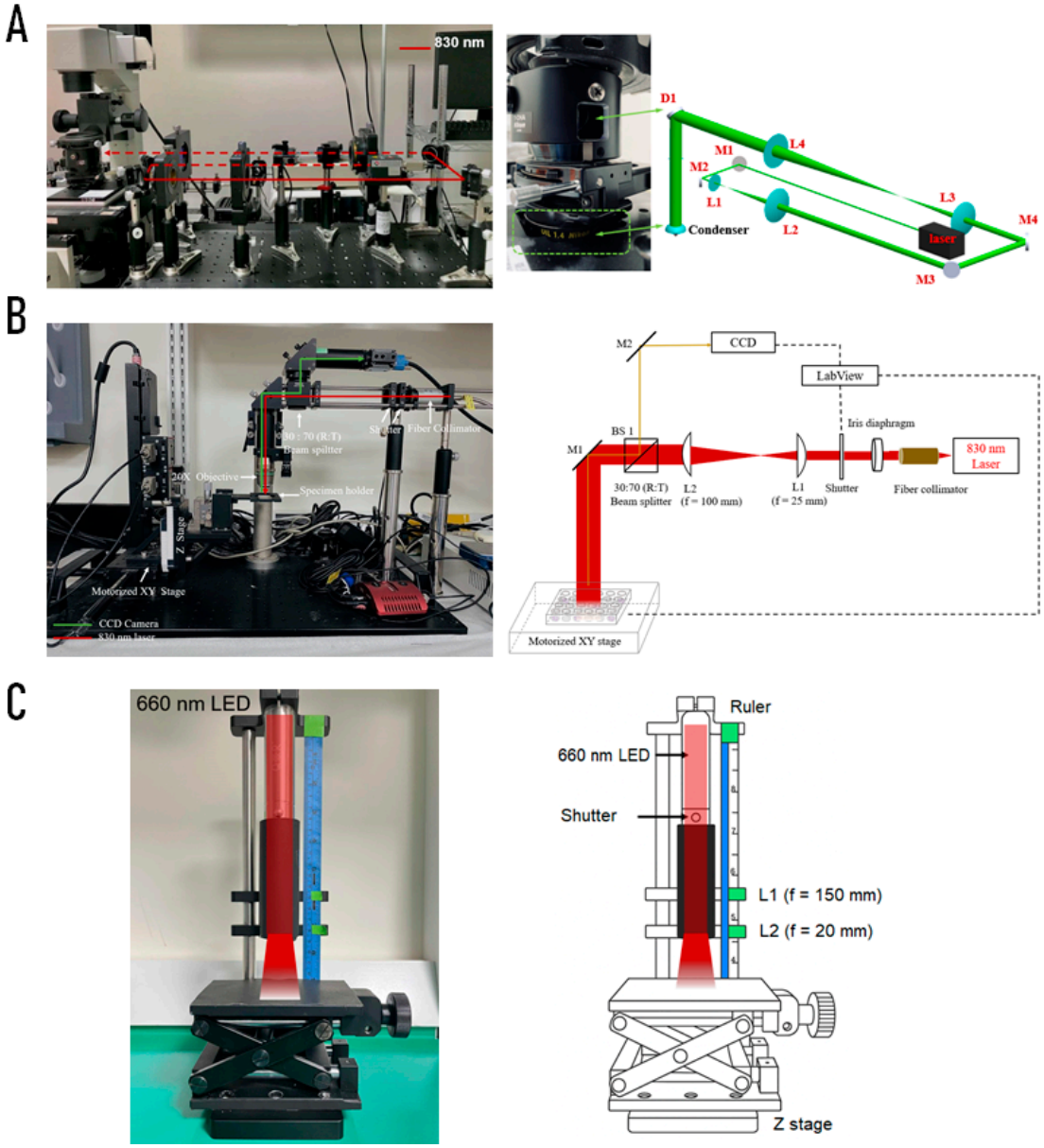

Figure 6. Experimental photobiomodulation (PBM) irradiation systems. (A) Custom-built 830 nm near-infrared (NIR) laser platform integrated with an inverted Nikon TE2000U microscope for single-cell irradiation and fluorescence imaging, with schematic of the optical path showing plano-convex lenses (L1–L4), mirrors (M1–M4), and dichroic mirror (D1). (B) Bulk-cell 830 nm NIR irradiation system used for viability and functional assays, consisting of a fiber-coupled laser diode, collimation optics (L1, L2), iris diaphragm, mechanical shutter, 30:70 (R:T) beam splitter, and CCD monitoring system mounted on a motorized XY stage, with schematic of beam delivery to multiwell plates. (C) Customized 660 nm LED irradiation system designed for uniform illumination, comprising a vertically mounted LED source, beam-shaping optics (L1 = 150 mm, L2 = 20 mm), mechanical shutter, and adjustable Z-stage, enabling stable and homogeneous fluence delivery across microchambers and multiwell culture formats.

4.2.1. PBM Dose Selection and Experimental Design

For both the 830 nm NIR laser and the 660 nm LED platforms, fluence ranges were selected according to the specific experimental format and biological endpoint, following a stepwise dose-screening strategy.

Single-cell experiments (microchamber platforms): For single-cell irradiation combined with live fluorescence imaging, three fluences were tested for both light sources: 2.5, 5.0, and 10.0 J/cm². These

© 2025 by the author(s). Distributed under a Creative Commons CC BY license.

Preprints.org (www.preprints.org) | NOT PEER-REVIEWED | Posted: 5 February 2026 doi:10.20944/preprints202602.0413.v1

experiments were designed to assess immediate mitochondrial membrane potential and redox responses within the same cell before and after PBM exposure, enabling identification of source-specific and dose-dependent mitochondrial effects at the individual cell level.

Bulk cell experiments (multiwell formats). For population-level assays, fluence ranges were adapted to the specific readout:

- Cell viability screening (96-well format). To more fully characterize biphasic dose–response behavior, bulk viability assays were performed using 2.5, 5.0, 10.0, and 15.0 J/cm² for both LED and NIR platforms.
- Mechanistic and functional assays (96- and 24-well formats).
  Based on concordant findings from single-cell mitochondrial assays and bulk viability screening, 5.0 J/cm² was identified as the most consistently effective fluence across both light sources. This dose was therefore selected for all subsequent functional studies, including ATP production (96-well), ROS signaling, migration, differentiation, and extracellular vesicle (EV) release (24-well format).

Dosimetry and Irradiation Control

For each optical configuration, beam geometry and alignment were fixed. Equivalent fluences were achieved by adjusting exposure time and illuminated area, while maintaining constant source output within each configuration. Fluence modulation was therefore accomplished exclusively through changes in exposure duration, as detailed in Table 3. Microchamber conditions correspond to confined irradiation for single-cell analyses, whereas 96-well and 24-well formats represent bulk population exposure.

Table 3. Photobiomodulation dosimetry parameters for single-cell and bulk irradiation formats using 660 nm LED and 830 nm NIR laser sources. Single-cell microchamber experiments were performed at 2.5, 5, and 10 J/cm² to evaluate dose-dependent mitochondrial responses. Bulk viability assays in 96-well plates included an extended fluence range (2.5–15 J/cm²) to assess biphasic effects. Based on these dose-screening experiments, 5 J/cm² was selected for subsequent functional assays in 24-well plates, including ROS, migration, differentiation, and extracellular vesicle analyses. Power output and illuminated area were constant within each optical configuration, and fluence was modulated by adjusting exposure time.

System & Light Source	Fluence (J/cm²)	Time (s)	Power (W)	Area (cm²)
Microchamber NIR 830 nm	2.5	27	0.0073	0.000008
	5.0	54		
	10.0	108		
Microchamber LED 660 nm (5 mm pinhole before L1)	2.5	27	0.0181	0.196
	5.0	54		
	10.0	108		
96-well NIR 830 nm	2.5	130	0.0073	0.38
	5.0	260		
	10.0	520		
	15.0	780		
96-well LED 660 nm (5 mm pinhole before L2)	2.5	28	0.034	0.38
	5.0	56		
	10.0	112		
	15.0	168		
24-well NIR 830 nm	5.0	32	0.311	2.01
24-well LED 660 nm	5.0	75	0.127	1.90

© 2025 by the author(s). Distributed under a Creative Commons CC BY license.

Preprints.org (www.preprints.org) | NOT PEER-REVIEWED | Posted: 5 February 2026 doi:10.20944/preprints202602.0413.v1

Real-time light output for each irradiation system was verified using a wavelength-adjusted thermal power sensor (PD300-3W-V1, Ophir, Israel), with calibration performed at the sample plane after accounting for optical transmission factors and confirmed before each experiment to ensure irradiance stability and reproducibility across experimental sessions.

All irradiations were conducted at ambient laboratory temperature (25 °C), with culture plates removed from the incubator only for the duration of light exposure to minimize environmental fluctuations. Irradiations were performed under controlled ambient lighting conditions, with overhead laboratory lights switched off so that samples were exposed exclusively to the designated PBM source, thereby avoiding unintended background photostimulation.

During LED-based experiments, only the target well or microchamber being irradiated was exposed at any given time, while all surrounding wells and non-treated samples, including control groups, were shielded with opaque covers to prevent exposure to scattered or reflected light during neighboring irradiations.

4.2.1. Single-Cell NIR Laser System (830 nm)

For single-cell experiments assessing mitochondrial membrane potential (ΔΨm/MMP) and reactive oxygen species (ROS), a custom-built 830 nm continuous-wave NIR laser platform was integrated into a Nikon TE2000U inverted microscope [35]. The collimated laser beam was expanded through a series of plano-convex lenses (L1–L4) and directed into the optical path by a dichroic mirror (D1). Mirrors (M1–M4) ensured alignment and beam delivery into a microfluidic chamber containing adherent C2C12 cells. This configuration enabled localized, high-resolution irradiation and real-time single-cell fluorescence imaging (Figure 6A).

In contrast to the LED configuration, the NIR laser system was focused to irradiate individual cells sequentially, enabling direct single-cell light delivery and post-irradiation imaging of the same targeted cells.

4.2.2. Bulk-Cell NIR Laser System (830 nm)

For population-level experiments (cell viability, migration, differentiation, and extracellular vesicle release), a separate 830 nm NIR laser system was employed [38]. The setup consisted of a fiber-coupled laser diode, collimation optics (L1, L2), iris diaphragm, and mechanical shutter. A 30:70 beam splitter directed part of the beam toward a CCD monitoring system, while the main beam illuminated cells cultured in 96 or 24 well plates mounted on a motorized XY stage. This arrangement allowed uniform dosing across multiple wells and facilitated automated treatment protocols (Figure 6B).

4.2.3. Customized LED System (660 nm)

For comparison with laser irradiation, a custom collimated LED system (660 nm) was constructed for photobiomodulation experiments, with optical conditioning inspired by the design reported by Baldassarro et al. [36] to ensure controlled irradiance, uniform illumination, and reproducibility. The LED source was mounted in a fixed metallic holder at the top of a vertical optical rail and remained stationary throughout all experiments (Oceanhood Taoyuan, Taiwan). Beam shaping and divergence control were achieved using two movable plano-convex lenses (L1 = 150 mm, L2 = 20 mm) mounted on adjustable carriers along the same rail [59].

An optical pinhole with a 5 mm diameter (ThorLabs ID12) was inserted when required to further constrain the beam profile for microchamber and 96-well plate irradiation. In the case of microchamber experiments, the pinhole was positioned immediately before L1; whereas for 96-well plate irradiation, it was positioned immediately before L2. Biological samples were placed on an adjustable Z-stage located beneath the optical train, allowing precise positioning of microchambers, 96-well plates, or 24-well plates at the desired focal distance. By adjusting the relative positions of L1, L2, and the Z-stage while keeping the LED source fixed, the illuminated field could be matched to

© 2025 by the author(s). Distributed under a Creative Commons CC BY license.

Preprints.org (www.preprints.org) | NOT PEER-REVIEWED | Posted: 5 February 2026 doi:10.20944/preprints202602.0413.v1

the required treatment area of each experimental format, ensuring consistent fluence delivery across both microchambers and culture plates (Table 3).

Exposure timing was controlled using a mechanical shutter, and fixed optical alignment ensured stable and repeatable irradiation geometry across experiments. This system was therefore used for both single-cell mitochondrial measurements and population-level functional assays, including viability, migration, differentiation, and extracellular vesicle analysis (Figure 6C).

For single-cell analyses under LED irradiation, the entire central microchamber field (0.196 cm^2) was uniformly illuminated, with mitochondrial and redox parameters subsequently quantified at the individual cell level (same cell pre and post treatment) by inverted fluorescence microscopy within the treated area.

Irradiance stability and spatial uniformity of the 660 nm LED output were monitored using an Ophir Starlite power meter to ensure consistent exposure conditions across experiments.

4.3. Single-Cell Assays of Mitochondrial Function and ROS

4.3.1. Mitochondrial Membrane Potential (ΔΨm)

Mithochondrial Membrane Potential was measured with Rhodamine 123 (Rh123; 5 µM, PromoCell GmbH) as described by Pan et al. [35] and validated as a ΔΨm probe [39,56]. Fluorescence intensity was acquired before irradiation (S_1) and 30 min post-irradiation (S_2), expressed as the S_2/S_1 ratio.

4.3.2. Intracellular ROS

Intracellular ROS were detected with H_2DCFDA (10 µM; Invitrogen D-399) before and 30 min after PBM. Data were analyzed as R_2/R_1 ratios [35], with interpretation guided by established ROS-detection frameworks [40,57,58]. Imaging was performed with an EMCCD camera (Andor LucaEM S658M) and quantified in MATLAB with local background subtraction [35].

4.4. Population Level Experiments

4.4.1. Cell Viability

Cell viability was determined using the Cell Counting Kit-8 (CCK-8; Elabscience, CCK-8 buffer, Cat# E-CK-A361) following published protocols [38]. C2C12 cells were seeded at 5 × 10^3/well in 96-well plates and irradiated at 0, 2.5, 5, or 10 J/cm^2 (LED or NIR). After 24 h, absorbance was measured at 450 nm using a microplate spectrophotometer (Agilent BioTek EPOCH2NS, USA).

4.4.2. Bulk ROS Measurement

Intracellular ROS levels in young (≤5 passages) and old (≥30 passages) C2C12 cells were assessed using the ROS-ID® Total ROS Detection Kit (Enzo Life Sciences, Cat# ENZ-51011). Cells were seeded at 1 × 10^5 cells per well in 24-well plates and allowed to adhere overnight. Following PBM irradiation with LED (660 nm) or NIR (830 nm) at the selected fluence of 5 J/cm^2, cells were incubated with 200 µL of ROS detection solution for 30 min, followed by the addition of 300 µL of ROS buffer (total 500 µL). Negative control wells received only ROS buffer without the detection dye, and positive controls received ROS inducer. Fluorescence was analyzed by flow cytometry (FACSDiscover S8; Ex = 488 nm, Em = 520 nm) to quantify ROS-positive cells across treatment groups. [59] The gating strategy and representative plots for ROS detection are provided in Supplementary Figures S1 and S2.

4.4.3. Bulk ATP Measurement

Cellular ATP content was measured using the ATPlite 1step Luminescence Assay System (Revvity, Cat# 6016736). Young (≤5 passages) and old (≥30 passages) C2C12 cells were seeded at 5 × 10^4 cells per well in 96-well plates and cultured overnight. After PBM irradiation with LED (660 nm)

© 2025 by the author(s). Distributed under a Creative Commons CC BY license.

Preprints.org (www.preprints.org) | NOT PEER-REVIEWED | Posted: 5 February 2026 doi:10.20944/preprints202602.0413.v1

or NIR (830 nm) at 5 J/cm², 100 µL of ATP detection reagent was added directly to each well according to the manufacturer's protocol. Plates were shaken for 20 s to ensure mixing, and luminescence was measured using a microplate reader. Relative ATP levels were normalized to control groups, with interpretation contextualized by ATP studies [59–61].

4.4.4. Migration Assay

Cell migration was evaluated using standardized culture-insert chambers (Ibidi, Germany), which generate a reproducible 500 µm cell-free gap [38]. Inserts were positioned in the outer wells of a 24-well plate to match the irradiation parameters optimized for this plate format. C2C12 myoblasts were seeded at a density of 3×10^4 cells per chamber side and allowed to form a confluent monolayer following 12 h incubation at 37 °C in 5% CO_2. Inserts were then carefully removed to create the defined wound area, and cultures were exposed to PBM (LED or NIR) at a fluence of 5 J/cm². To minimize the contribution of proliferation and isolate migration, cultures were maintained in serum-free DMEM immediately after PBM. At 12 h post-irradiation, the medium was replaced with low-serum DMEM containing 2% FBS for the remainder of the assay [62]. Bright-field images (4× objective) of gap closure were acquired at 0, 12, 16, 24, 36, and 48 h post-treatment using an inverted microscope (Leica DMi8, Germany). Migration dynamics were quantified as percentage gap closure over time using ImageJ (by an investigator blinded to experimental conditions). All experiments were performed in triplicate to ensure reproducibility.

Wound Closure Quantification

The wound area was measured using ImageJ software (NIH, USA), and values were normalized to the initial wound size at 0 h [63].

- Relative gap (%):

The remaining wound area at time t expressed as a percentage of the baseline gap:

$$\text{Relative gap (\%)} = \frac{W_t}{W_0} \times 100 \tag{2}$$

where W_0 is the wound gap at 0 h and W_t is the gap at time t.

- Relative closure rate (%/h):

The average rate of closure from baseline to a given time point, expressed as percent reduction in relative gap per hour:

$$\text{Relative closure rate (\%/h)} = \frac{100 - \text{Relative gap at time } t}{\Delta t} \tag{3}$$

where Δt is the elapsed time (h) since 0 h.

- Interval-specific closure rate (%/h):

The rate of closure calculated between two consecutive time points, reflecting dynamic changes across different phases of migration:

$$\text{Interval closure rate (\%/h)} = \frac{\text{Relative gap at start} - \text{Relative gap at end}}{\Delta t} \tag{4}$$

where "start" and "end" represent two successive measurement times.

All experiments were performed in triplicate, and results were expressed as mean ± SEM.

4.4.5. Differentiation Assay

Differentiation was induced as previously described in the Cell Culture Methods section. Cells were subsequently stained with Hoechst 33342 for nuclear visualization. For each condition, images were acquired in both bright-field and fluorescence (Hoechst) channels using identical exposure times and magnification settings across all groups. Bright-field images were used to evaluate myotube morphology, while co-registered Hoechst fluorescence images were used to delineate nuclei

© 2025 by the author(s). Distributed under a Creative Commons CC BY license.

Preprints.org (www.preprints.org) | NOT PEER-REVIEWED | Posted: 5 February 2026 doi:10.20944/preprints202602.0413.v1

(Leica DMi8 manual inverted microscope, Germany). Multiple non-overlapping fields were analyzed per well across at least three independent experiments.

In each field, the total number of nuclei (N_total) was first determined. Multinucleated myotubes were then identified based on morphological criteria, defined as elongated fibers containing two or more Hoechst-positive nuclei within a continuous cytoplasm and clearly separated from adjacent cells. Nuclei located within these myotubes were counted as N_MT. The fusion index (FI) was calculated as:

$$\text{FI}\,(\%) = \frac{\text{N\_MT}}{\text{N\_total}} \times 100 \quad (5)$$

All counts were performed by a blinded rater, and discrepancies were reconciled by joint review. Adapted from established protocols [18,64,65].

4.4.5. Extracellular Vesicle Isolation and Characterization

For extracellular vesicle (EV) isolation, C2C12 myoblasts at early passage (P ≤ 5) or late passage (P ≥ 30) were seeded in 24-well tissue-culture plates at a density of 5×10^4 cells per well and allowed to adhere overnight at 37 °C with 5% CO_2. Conditioned medium was collected 24 h after PBM exposure (5 J/cm² using either the 660 nm LED or 830 nm NIR laser system) under serum-free conditions. EVs were isolated by differential centrifugation followed by ultracentrifugation [38,47], with all steps performed at 4 °C. Supernatants were sequentially cleared at 200× g for 10 min, 2,000× g for 10 min, and 10,000× g for 30 min, retaining the supernatant at each step. The final supernatant was then ultracentrifuged at 100,000× g for 70 min, and the EV pellet was resuspended in 0.1 µm-filtered PBS for downstream analyses and storage at −80 °C.

Particle size distribution and concentration were quantified by nanoparticle tracking analysis (NTA; NanoSight NS300, Malvern) using a 532 nm laser. Instrument settings and acquisition duration were kept constant across all groups, and measurements were conducted at concentrations yielding 20 to 100 particles per frame to ensure robust tracking. Each sample was measured in technical triplicate using 60 s video acquisitions, and values were averaged. For each experimental condition, conditioned medium from three wells of a 24-well plate was pooled for NTA analysis.

Surface tetraspanin profiling was performed using the ExoView R200 platform with the Leprechaun Exosome Mouse Tetraspanin Kit to detect CD9, CD63, and CD81. Sample input concentrations were adjusted to 1×10^7- 1×10^9 EVs/mL based on NTA results. Chips were processed and analyzed according to the manufacturer's instructions, and particle counts per capture spot as well as fluorescence-confirmed subpopulations were quantified. This platform was selected because it preserves vesicle integrity, enables single-particle resolution, and has been applied in PBM studies to confirm consistency in EV size and marker expression between PBM-treated and control samples [66].

The overall PBM-EV experimental framework was aligned with recent mechanistic studies of biophysical stimulation [67–69] and PBM-based tissue and cell models [38,47,59,70].

4.5. Statistical Analysis

All experiments were performed with ≥3 biological replicates. Data are presented as mean ± SEM. Group comparisons were analyzed by one-way ANOVA followed by Tukey's post hoc test. Statistical significance was set at $p < 0.05$. Graphs and statistical outputs were generated with GraphPad Prism 8.

5. Conclusions

This study demonstrates that photobiomodulation at 660 nm (LED) and 830 nm (NIR) activates mitochondrial and redox signaling in C2C12 myoblasts in a fluence-dependent manner, while eliciting distinct functional outcomes shaped by irradiation source and replicative age. Despite comparable single-cell mitochondrial polarization and mitohormetic ROS signaling, LED and NIR

© 2025 by the author(s). Distributed under a Creative Commons CC BY license.

Preprints.org (www.preprints.org) | NOT PEER-REVIEWED | Posted: 5 February 2026 doi:10.20944/preprints202602.0413.v1

diverged at the population level, indicating that early bioenergetic activation does not directly predict downstream myogenic behavior. LED preferentially supported metabolic and ATP-associated responses, particularly in aged cells, whereas NIR consistently enhanced myogenic fusion and differentiation efficiency across age groups. These findings highlight replicative stage as a critical determinant of how mitochondrial signals are translated into functional outputs. Collectively, our data provide a mechanistic basis for tailoring photobiomodulation parameters and sources to specific myogenic objectives and support age-adapted PBM strategies for muscle regeneration research.

Supplementary Materials: The following supporting information can be downloaded at the website of this paper posted on Preprints.org.

Author Contributions: Author Contributions: Conceptualization, A.E.A., Y.Y., C.-J.C. and T.-S.Y.; methodology, A.E.A., Y.-F.C., A.Y.L.W., C.-J.C. and T.-S.Y.; investigation, A.E.A., N.L.T.H. and C.-Y.C.; validation, C.-Y.C. and X.P.-C.W.; data curation, A.E.A. and N.L.T.H.; formal analysis and data interpretation, A.E.A. and X.P.-C.W.; visualization, A.E.A. and N.L.T.H.; resources, Y.-F.C. and A.Y.L.W.; writing:original draft preparation, A.E.A.; writing:review and editing, T.-S.Y.; supervision, Y.-F.C., Y.Y., C.-J.C. and T.-S.Y.; project administration, Y.Y., C.-J.C. and T.-S.Y.; funding acquisition, C.-J.C. and T.-S.Y. All authors have read and agreed to the published version of the manuscript.

Funding: This research was supported by the Ministry of Education, Taiwan (grant numbers DP2-TMU-112-O-04 and DP2-TMU-113-O-05) and the National Science and Technology Council (NSTC), Taiwan (grant number NSTC 114-2221-E-038-006) to T.-S.Y., and by the National Science and Technology Council (NSTC), Taiwan (grant number 112-5400-020-400) to C.-J.C.

Institutional Review Board Statement: Not applicable.

Informed Consent Statement: Not applicable.

Data Availability Statement: The original contributions presented in this study are included in the article/supplementary material. Further inquiries can be directed to the corresponding authors.

Acknowledgments: The authors extend their sincere gratitude to all individuals and institutions who contributed to this study. We acknowledge the assistance of Kate Ming-Yu Chuang (medical student) and Evan Yuan-Hao Chen (prospective undergraduate student) during experimental procedures and data collection. The authors also thank the Biophotonics Laboratory members at Taipei Medical University for technical support and constructive discussions.

Conflicts of Interest: The authors declare no conflict of interest. The authors declare that no financial or personal relationships exist that could be perceived to have influenced the work reported in this article.

Abbreviations

The following abbreviations are used in this manuscript:

ANOVA	Analysis of Variance
ATP	Adenosine Triphosphate
CCK-8	Cell Counting Kit-8
CcO	Cytochrome c Oxidase
CO_2	Carbon Dioxide
DMEM	Dulbecco's Modified Eagle Medium
DMSO	Dimethyl Sulfoxide
$\Delta\Psi m$	Mitochondrial Membrane Potential
EMCCD	Electron-Multiplying Charge-Coupled Device
ESCRT	Endosomal Sorting Complex Required for Transport
EV	Extracellular Vesicle
FACS	Fluorescence-Activated Cell Sorting
FBS	Fetal Bovine Serum

© 2025 by the author(s). Distributed under a Creative Commons CC BY license.

Preprints.org (www.preprints.org) | NOT PEER-REVIEWED | Posted: 5 February 2026 doi:10.20944/preprints202602.0413.v1

FI	Fusion Index
LED	Light-Emitting Diode
MAPK	Mitogen-Activated Protein Kinase
MMP	Mitochondrial Membrane Potential
NIR	Near-Infrared
NTA	Nanoparticle Tracking Analysis
PBM	Photobiomodulation
Rh123	Rhodamine 123
ROS	Reactive Oxygen Species
SEM	Standard Error of the Mean

References

1. Anders, J.J.; Lanzafame, R.J.; Arany, P.R. Low-level light/laser therapy versus photobiomodulation therapy. *Photomed. Laser Surg.* **2015**, *33*, 183–184. https://doi.org/10.1089/pho.2015.9848
2. Hamblin, M.R. Mechanisms and mitochondrial redox signaling in photobiomodulation. *Photochem. Photobiol.* **2018**, *94*, 199–212. https://doi.org/10.1111/php.12864
3. Karu, T.I. Primary and secondary mechanisms of action of visible to near-IR radiation on cells. *J. Photochem. Photobiol. B* **1999**, *49*, 1–17. https://doi.org/10.1016/S1011-1344(98)00219-X
4. Karu, T.I.; Kolyakov, S.F. Exact action spectra for cellular responses relevant to phototherapy. *Photomed. Laser Surg.* **2005**, *23*, 355–361. https://doi.org/10.1089/pho.2005.23.355
5. Sarti, P.; Forte, E.; Mastronicola, D.; Giuffrè, A.; Arese, M. Cytochrome c oxidase and nitric oxide in action: Molecular mechanisms and pathophysiological implications. *Biochim. Biophys. Acta Bioenerg.* **2012**, *1817*, 610–619. https://doi.org/10.1016/j.bbabio.2011.09.002
6. Mochizuki-Oda, N.; Kataoka, Y.; Cui, Y.; Yamada, H.; Heya, M. Effects of near-infrared laser irradiation on adenosine triphosphate and adenosine diphosphate contents of rat brain tissue. *Neurosci. Lett.* **2002**, *323*, 207–209. https://doi.org/10.1016/S0304-3940(02)00159-3
7. Sies, H.; Jones, D.P. Reactive oxygen species (ROS) as pleiotropic physiological signalling agents. *Nat. Rev. Mol. Cell Biol.* **2020**, *21*, 363–383. https://doi.org/10.1038/s41580-020-0230-3
8. Zorov, D.B.; Juhaszova, M.; Sollott, S.J. Mitochondrial reactive oxygen species (ROS) and ROS-induced ROS release. *Physiol. Rev.* **2014**, *94*, 909–950. https://doi.org/10.1152/physrev.00026.2013
9. Turrens, J.F. Mitochondrial formation of reactive oxygen species. *J. Physiol.* **2003**, *552*, 335–344. https://doi.org/10.1111/j.1469-7793.2003.00335.x
10. Murphy, M.P. How mitochondria produce reactive oxygen species. *Biochem. J.* **2009**, *417*, 1–13. https://doi.org/10.1042/BJ20081386
11. Divakaruni, A.S.; Brand, M.D. The regulation and physiology of mitochondrial proton leak. *Physiol. Rev.* **2011**, *91*, 793–829. https://doi.org/10.1152/physiol.00046.2010
12. Korshunov, S.S.; Skulachev, V.P.; Starkov, A.A. High protonic potential actuates a mechanism of production of reactive oxygen species in mitochondria. *FEBS Lett.* **1997**, *416*, 15–18. https://doi.org/10.1016/S0014-5793(97)01159-9
13. Ferraresi, C.; Hamblin, M.R.; Parizotto, N.A. Low-level laser (light) therapy on muscle tissue: Performance, fatigue and repair benefited by the power of light. *Photonics Lasers Med.* **2012**, *5*, 247–261. https://doi.org/10.1515/plm-2012-0032
14. Leal-Junior, E.C.P.; Vanin, A.A.; Miranda, E.F.; de Carvalho, P.D.T.C.; Dal Corso, S. Effect of phototherapy (low-level laser therapy and light-emitting diode therapy) on exercise performance and markers of exercise recovery: A systematic review with meta-analysis. *Lasers Med. Sci.* **2015**, *30*, 925–939. https://doi.org/10.1007/s10103-013-1465-4
15. Huang, Y.Y.; Sharma, S.K.; Carroll, J.; Hamblin, M.R. Biphasic dose response in low level light therapy - an update. *Dose Response* **2011**, *9*, 602–618. https://doi.org/10.2203/dose-response.11-009.Hamblin
16. Silveira, P.C.L.; Streck, E.L.; Pinho, R.A. Evaluation of mitochondrial respiratory chain activity in muscle healing by low-level laser therapy. *J. Photochem. Photobiol. B* **2009**, *95*, 89–92. https://doi.org/10.1016/j.jphotobiol.2009.01.004

© 2025 by the author(s). Distributed under a Creative Commons CC BY license.

Preprints.org (www.preprints.org) | NOT PEER-REVIEWED | Posted: 5 February 2026 doi:10.20944/preprints202602.0413.v1

17. Gholami, L.; Khorsandi, K.; Nooshabadi, V.T.; Shahabi, S.; Jazaeri, M.; Esfahani, H.; Faradonbeh, D.R.; Malekshahi, Z.V.; Afsartala, Z.; Mostafa, N. Effect of photobiomodulation on structure and function of extracellular vesicle secreted from mesenchymal stem cells. *Photochem. Photobiol.* **2022**, *98*, 1447–1458. https://doi.org/10.1111/php.13633
18. Lovisetto, R.; Malavazzi, T.C.S.; Andreo, L.; Rodrigues, M.F.S.D.; Bussadori, S.K.; Fernandes, K.P.S.; Mesquita-Ferrari, R.A. Photobiomodulation using different infrared light sources promotes muscle precursor cells migration and proliferation. *Photonics* **2022**, *9*, 469. https://doi.org/10.3390/photonics9070469
19. Vechetti, I.J., Jr.; Valentino, T.; Mobley, C.B.; McCarthy, J.J. The role of extracellular vesicles in skeletal muscle and systemic adaptation to exercise. *J. Physiol.* **2021**, *599*, 845–861. https://doi.org/10.1113/JP278929
20. da Silva, E.M.; Mesquita-Ferrari, R.A.; Rodrigues, M.F.S.D.; Magalhães, E.M.R.; Bussadori, S.K.; de Brito, A.; Messias, F.D.M.; Souza, N.H.C.; Alves, A.N.; Fernandes, K.P.S. The effects of photobiomodulation on inflammatory infiltrate during muscle repair in advanced-age rats. *J. Gerontol. A Biol. Sci. Med. Sci.* **2020**, *75*, 437–441. https://doi.org/10.1093/gerona/glz076
21. Coen, P.M.; Musci, R.V.; Hinkley, J.M.; Miller, B.F. Mitochondria as a target for mitigating sarcopenia. *Front. Physiol.* **2019**, *9*, 1883. https://doi.org/10.3389/fphys.2018.01883
22. Short, K.R.; Bigelow, M.L.; Kahl, J.; Singh, R.; Coenen-Schimke, J.; Raghavakaimal, S.; Nair, K.S. Decline in skeletal muscle mitochondrial function with aging in humans. *Proc. Natl. Acad. Sci. USA* **2005**, *102*, 5618–5623. https://doi.org/10.1073/pnas.0501559102
23. Rygiel, K.A.; Picard, M.; Turnbull, D.M. The ageing neuromuscular system and sarcopenia: A mitochondrial perspective. *J. Physiol.* **2016**, *594*, 4499–4512. https://doi.org/10.1113/JP271212
24. Chen, L.K.; Woo, J.; Assantachai, P.; et al. Asian Working Group for Sarcopenia: 2019 consensus update on sarcopenia diagnosis and treatment. *J. Am. Med. Dir. Assoc.* **2020**, *21*, 300–307.e2. https://doi.org/10.1016/j.jamda.2019.12.012
25. Girasol, C.E.; Moraes, J.M.A.F.; Bachmann, L.; Alfredo, D.M.N.; Barbosa, R.I.; Guirro, E.C.O.; Guirro, R.R.J. In vivo attenuation profile of 660 nm and 830 nm wavelengths on human elbow skin and calcaneus tendon of different phototypes. *Lasers Med. Sci.* **2024**, *39*, 24. https://doi.org/10.1007/s10103-023-03955-3
26. de Lima, E.V.; Pacheco-Soares, C.; da Silva, N.S. Photobiomodulation assay of muscle cells C2C12 after irradiation with LED device. *Res. Soc. Dev.* **2022**, *11*, e41511628884. https://doi.org/10.33448/rsd-v11i6.28884
27. Oyebode, O.A.; Houreld, N.N. A comparison between photobiomodulation at 830 nm and 660 nm on differentiation in diabetic human skin fibroblast cells. In *Proceedings of the SAIP2021 Conference*, South Africa, **2021**; pp. 1–6. https://saip.org.za/Proceedings/Track%20C/41.pdf
28. Desmet, K.D.; Paz, D.A.; Corry, J.J.; et al. Clinical and experimental applications of NIR-LED photobiomodulation. *Photomed. Laser Surg.* **2006**, *24*, 121–128. https://doi.org/10.1089/pho.2006.24.121
29. Ferro, A.P.; de Jesus Guirro, R.R.; Orellana, M.D.; De Santis, G.C.; Farina, J.A., Jr.; de Oliveira Guirro, E.C. Photobiomodulation with laser and LED on mesenchymal stem cells viability and wound closure in vitro. *Lasers Med. Sci.* **2024**, *39*, 205. https://doi.org/10.1007/s10103-024-04159-z
30. Heiskanen, V.; Hamblin, M.R. Photobiomodulation: Lasers vs. light-emitting diodes? *Photochem. Photobiol. Sci.* **2018**, *17*, 1003–1017. https://doi.org/10.1039/C8PP00176F
31. Yaffe, D.; Saxel, O. Serial passaging and differentiation of myogenic cells isolated from dystrophic mouse muscle. *Nature* **1977**, *270*, 725–727. https://doi.org/10.1038/270725a0
32. Burattini, S.; Ferri, P.; Battistelli, M.; Curci, R.; Luchetti, F.; Falcieri, E. C2C12 murine myoblasts as a model of skeletal muscle development: Morpho-functional characterization. *Eur. J. Histochem.* **2004**, *48*, 223–233. https://doi.org/10.4081/891
33. Potes, Y.; Bermejo-Millo, J.C.; Mendes, C.; Castelão-Baptista, J.P.; Díaz-Luis, A.; Pérez-Martínez, Z.; Solano, J.J.; Sardão, V.A.; Oliveira, P.J.; Caballero, B.; Coto-Montes, A. p66Shc signaling and autophagy impact on C2C12 myoblast differentiation during senescence. *Cell Death Dis.* **2024**, *15*, 200. https://doi.org/10.1038/s41419-024-06582-0
34. Rahman, F.A.; Hian-Cheong, D.J.; Boonstra, K.; Ma, A.; Thoms, J.P.; Zago, A.S.; Quadrilatero, J. Augmented mitochondrial apoptotic signaling impairs C2C12 myoblast differentiation following cellular aging through sequential passaging. *J. Cell. Physiol.* **2024**, *239*, e31155. https://doi.org/10.1002/jcp.31155

© 2025 by the author(s). Distributed under a Creative Commons CC BY license.

Preprints.org (www.preprints.org) | NOT PEER-REVIEWED | Posted: 5 February 2026 doi:10.20944/preprints202602.0413.v1

35. Pan, L.C.; Hang, N.L.T.; Colley, M.M.S.; Chang, J.; Hsiao, Y.C.; Lu, L.S.; Li, B.S.; Chang, C.J.; Yang, T.S. Single-cell effects of photobiomodulation on mitochondrial membrane potential and reactive oxygen species production in human adipose mesenchymal stem cells. *Cells* **2022**, *11*, 972. https://doi.org/10.3390/cells11060972
36. Baldassarro, V.A.; Alastra, G.; Lorenzini, L.; Giardino, L.; Calzà, L. Photobiomodulation at defined wavelengths regulates mitochondrial membrane potential and redox balance in skin fibroblasts. *Oxid. Med. Cell. Longev.* **2023**, *2023*, 7638223. https://doi.org/10.1155/2023/7638223
37. Ristow, M.; Schmeisser, K. Mitohormesis: Promoting health and lifespan by increased levels of reactive oxygen species (ROS). *Dose Response* **2014**, *12*, 288–341. https://doi.org/10.2203/dose-response.13-035.Ristow
38. Chang, C.Y.; Aviña, A.E.; Chang, C.J.; Lu, L.S.; Chong, Y.Y.; Ho, T.Y.; Yang, T.S. Exploring the biphasic dose–response effects of photobiomodulation on the viability, migration, and extracellular vesicle secretion of human adipose mesenchymal stem cells. *J. Photochem. Photobiol. B* **2024**, *256*, 112940. https://doi.org/10.1016/j.jphotobiol.2024.112940
39. Zorova, L.D.; Popkov, V.A.; Plotnikov, E.Y.; et al. Mitochondrial membrane potential. *Cell Death Dis.* **2018**, *9*, 950. https://doi.org/10.1016/j.ab.2017.07.009
40. Suski, J.M.; Lebiedzinska, M.; Bonora, M.; et al. Relation between mitochondrial membrane potential and ROS formation. *Methods Mol. Biol.* **2012**, *810*, 183–205. https://doi.org/10.1007/978-1-61779-382-0_12
41. Scaduto, R.C.; Grotyohann, L.W. Measurement of mitochondrial membrane potential using fluorescent rhodamine derivatives. *Biophys. J.* **1999**, *76*, 469–477. https://doi.org/10.1016/S0006-3495(99)77214-0
42. Brown, A.D.; Stewart, C.E.; Burniston, J.G. Degradation of ribosomal and chaperone proteins is attenuated during the differentiation of replicatively aged C2C12 myoblasts. *J. Cachexia Sarcopenia Muscle* **2022**, *13*, 2562–2575. https://doi.org/10.1002/jcsm.13034
43. Shintani-Ishida, K.; Tsurumi, R.; Ikegaya, H. Decrease in the expression of muscle-specific miRNAs, miR-133a and miR-1, in myoblasts with replicative senescence. *PLoS ONE* **2023**, *18*, e0280527. https://doi.org/10.1371/journal.pone.0280527
44. Hawke, T.J.; Garry, D.J. Myogenic satellite cells: Physiology to molecular biology. *J. Appl. Physiol.* **2001**, *91*, 534–551. https://doi.org/10.1152/jappl.2001.91.2.534
45. Barbieri, E.; Sestili, P. Reactive oxygen species in skeletal muscle signaling. *J. Signal Transduct.* **2012**, *2012*, 982794. https://doi.org/10.1155/2012/982794
46. Lian, D.; Chen, M.M.; Wu, H.; Deng, S.; Hu, X. The role of oxidative stress in skeletal muscle myogenesis and muscle disease. *Antioxidants* **2022**, *11*, 755. https://doi.org/10.3390/antiox11040755
47. Hang, N.L.T.; Chuang, A.E.Y.; Chang, C.J.; Yen, Y.; Wong, C.C.; Yang, T.S. Photobiomodulation associated with alginate-based engineered tissue on promoting chondrocytes-derived biological responses for cartilage regeneration. *Int. J. Biol. Macromol.* **2024**, *280*, 135982. https://doi.org/10.1016/j.ijbiomac.2024.135982
48. Murata, A.; Yamaguchi, Y.; Ueda, Y.; et al. Electrical pulse stimulation-induced tetanic exercise simulation increases the secretion of extracellular vesicles from C2C12 myotubes. *Biochem. Biophys. Res. Commun.* **2023**, *672*, 177–184. https://doi.org/10.1016/j.bbrc.2023.06.054
49. de Freitas, L.F.; Hamblin, M.R. Proposed mechanisms of photobiomodulation or low-level light therapy. *IEEE J. Sel. Top. Quantum Electron.* **2016**, *22*, 348–364. https://doi.org/10.1109/JSTQE.2016.2561201
50. Silveira, P.C.L.; Ferreira, G.K.; Zaccaron, R.P.; Remor, A.P.; da Silva, L.A.; Pinho, R.A. Effects of photobiomodulation on mitochondria of brain, muscle, and C6 astroglioma cells. *Med. Eng. Phys.* **2019**, *71*, 108–113. https://doi.org/10.1016/j.medengphy.2019.05.008
51. Frangini, M.; Franzolin, E.; Chemello, F.; Laveder, P.; Romualdi, C.; Bianchi, V.; Rampazzo, C. Synthesis of mitochondrial DNA precursors during myogenesis: An analysis in purified C2C12 myotubes. *J. Biol. Chem.* **2013**, *288*, 5624–5635. https://doi.org/10.1074/jbc.M112.441147
52. Parisi, B.; Sünnen, M.; Chippalkatti, R.; Abankwa, D.K. A flow-cytometry-based pipeline for the rapid quantification of C2C12 cell differentiation. *STAR Protoc.* **2023**, *4*, 102637. https://doi.org/10.1016/j.xpro.2023.102637

© 2025 by the author(s). Distributed under a Creative Commons CC BY license.

Preprints.org (www.preprints.org) | NOT PEER-REVIEWED | Posted: 5 February 2026 doi:10.20944/preprints202602.0413.v1

53. Tannu, N.S.; Rao, V.K.; Chaudhary, R.M.; Giorgianni, F.; Saeed, A.E.; Gao, Y.; Raghow, R. Comparative proteomes of the proliferating C2C12 myoblasts and fully differentiated myotubes reveal the complexity of the skeletal muscle differentiation program. *Mol. Cell. Proteomics* **2004**, *3*, 1065–1082. https://doi.org/10.1038/nprot.2006.256
54. Timmons, J.A.; Larsson, O.; Jansson, E.; Fischer, H.; Gustafsson, T.; Greenhaff, P.L.; Ridden, J.; Rachman, J.; Peyrard-Janvid, M.; Wahlestedt, C.; Sundberg, C.J. Human muscle gene expression responses to endurance training provide a novel perspective on Duchenne muscular dystrophy. *FASEB J.* **2005**, *19*, 750–760. https://doi.org/10.1096/fj.04-1980com
55. Wang, Y.; Liu, S.; Yan, Y.; Li, S.; Tong, H. SPARCL1 promotes C2C12 cell differentiation via BMP7-mediated BMP/TGF-β cell signaling pathway. *Cell Death Dis.* **2019**, *10*, 852. https://doi.org/10.1038/s41419-019-2049-4
56. Bortoletto, R.; Silva, N.S.; Zangaro, R.A.; Pacheco, M.T.T.; Da Matta, R.A.; Pacheco-Soares, C. Mitochondrial membrane potential after low-power laser irradiation. *Lasers Med. Sci.* **2004**, *18*, 204–206. https://doi.org/10.1007/s10103-003-0281-7
57. Groeger, G.; Quiney, C.; Cotter, T.G. Hydrogen peroxide as a cell-survival signaling molecule. *Antioxid. Redox Signal.* **2009**, *11*, 2655–2671. https://doi.org/10.1089/ars.2009.2728
58. Zhao, R.Z.; Jiang, S.; Zhang, L.; Yu, Z.B. Mitochondrial electron transport chain, ROS generation and uncoupling. *Int. J. Mol. Med.* **2019**, *44*, 3–15. https://doi.org/10.3892/ijmm.2019.4188
59. Aviña, A.E.; Chen, E.Y.H.; Chuang, K.M.Y.; Chang, C.Y.; Chang, C.J.; Yang, T.S. Safe Mitochondrial Activation through Photobiomodulation: Distinct Red and Near-Infrared Responses in Normal and Malignant Cells. *J. Biophotonics* 2025, e202500555. https://doi.org/10.1002/jbio.202500555
60. Imamura, H.; Huynh Nhat, K.P.; Togawa, H.; Saito, K.; Iino, R.; Kato-Yamada, Y.; Nagai, T.; Noji, H. Visualization of ATP levels inside single living cells with fluorescence resonance energy transfer-based genetically encoded indicators. *Proc. Natl. Acad. Sci. USA* **2009**, *106*, 15651–15656. https://doi.org/10.1073/pnas.0904764106
61. van Hameren, G.; Campbell, G.; Deck, M.; Berthelot, J.; Gautier, B.; Quintana, P.; Chrast, R.; Tricaud, N. In vivo real-time dynamics of ATP and ROS production in axonal mitochondria show decoupling in mouse models of peripheral neuropathies. *Acta Neuropathol. Commun.* **2019**, *7*, 86. https://doi.org/10.1186/s40478-019-0740-4
62. Hour, T.C.; Vo, T.C.T.; Chuu, C.P.; Chang, H.W.; Su, Y.F.; Chen, C.H.; Chen, Y.K. The promotion of migration and myogenic differentiation in skeletal muscle cells by quercetin and underlying mechanisms. *Nutrients* **2022**, *14*, 4106. https://doi.org/10.3390/nu14194106
63. Grada, A.; Otero-Viñas, M.; Prieto-Castrillo, F.; Obagi, Z.; Falanga, V. Research techniques made simple: Analysis of collective cell migration using the wound healing assay. *J. Investig. Dermatol.* **2017**, *137*, e11–e16. https://doi.org/10.1016/j.jid.2016.11.020
64. Wang, Z.; Ongkosuwito, E.M.; Von den Hoff, J.W.; Wagener, F.A. The effects of TGF-β receptor I inhibitors on myofibroblast differentiation and myotube formation. *Front. Cell Dev. Biol.* **2025**, *13*, 1636884. https://doi.org/10.3389/fcell.2025.1636884
65. Nguyen, M.T.; Ly, Q.K.; Ngo, T.H.P.; Lee, W. Calponin 3 regulates myoblast proliferation and differentiation through actin cytoskeleton remodeling and YAP1-mediated signaling in myoblasts. *Cells* **2025**, *14*, 142. https://doi.org/10.3390/cells14020142
66. Breitwieser, K.; Voglstaetter, M.; Stockner, T.; Boeck, T.; Scheiflinger, F.; Binder, C.J. Detailed characterization of small extracellular vesicles from different cell types based on tetraspanin composition by ExoView R100 platform. *Int. J. Mol. Sci.* **2022**, *23*, 8544. https://doi.org/10.3390/ijms23158544
67. Debbi, L.; Zohar, R.; Shilo, S.; et al. Boosting extracellular vesicle secretion. *Trends Biotechnol.* **2022**, *40*, 1239–1257. https://doi.org/10.1016/j.biotechadv.2022.107983
68. Guo, S.C.; Tao, S.C.; Yin, W.J.; Qi, X.; Yuan, T.; Zhang, C.Q. Exosomes derived from platelet-rich plasma promote the re-epithelization of chronic cutaneous wounds via activation of YAP in a diabetic rat model. *Theranostics* **2017**, *7*, 81. https://doi.org/10.7150/thno.16803

© 2025 by the author(s). Distributed under a Creative Commons CC BY license.

Preprints.org (www.preprints.org) | NOT PEER-REVIEWED | Posted: 5 February 2026 doi:10.20944/preprints202602.0413.v1

69. Fukuta, T.; Nishikawa, A.; Kogure, K. Low level electricity increases the secretion of extracellular vesicles from cultured cells. *Biochem. Biophys. Rep.* **2020**, *21*, 100713. https://doi.org/10.1016/j.bbrep.2019.100713
70. Dompe, C.; Moncrieff, L.; Matys, J.; Grzech-Leśniak, K.; Kocherova, I.; Bryja, A.; Bruska, M.; Dominiak, M.; Mozdziak, P.; Skiba, T.H.I. Photobiomodulation: Underlying mechanisms and clinical applications. *J. Clin. Med.* **2020**, *9*, 1724. https://doi.org/10.3390/jcm9061724

Disclaimer/Publisher's Note: The statements, opinions and data contained in all publications are solely those of the individual author(s) and contributor(s) and not of MDPI and/or the editor(s). MDPI and/or the editor(s) disclaim responsibility for any injury to people or property resulting from any ideas, methods, instructions or products referred to in the content.

© 2025 by the author(s). Distributed under a Creative Commons CC BY license.